electronics

MDPI

Article

Demonstration of Grid-Forming Controls in Hybrid AC/DC Grid in a Real-Time PHiL Environment

Michael Richter [1,†], Ananya Kuri [1,2,†], Julian Richter [1], Timo Wagner [1], Stefan Henninger [3] and Gert Mehlmann [1,*]

1 Institute for Electrical Energy Systems, Friedrich-Alexander Universität Erlangen-Nürnberg, 91058 Erlangen, Germany; michael.m.richter@fau.de (M.R.); ananya.kuri@fau.de (A.K.); julian.richter@fau.de (J.R.); timo.wagner@fau.de (T.W.)
2 Siemens AG Foundational Technologies, 91058 Erlangen, Germany
3 Fluence Energy GmbH, 91056 Erlangen, Germany
* Correspondence: gert.mehlmann@fau.de
† These authors contributed equally to this work.

Abstract: The transition to inverter-dominated power systems with novel control strategies has created weak grid scenarios, prompting extensive research into grid-forming (GFM) converters and advanced GFM control schemes. This study evaluates two GFM control strategies for their stabilizing effects in weakly interconnected and islanded power systems: the established Virtual Synchronous Machine (VSM) control and the newly developed Phase-Restoring Principle (PRP). The evaluation is conducted using a real-time electromagnetic transient (EMT) simulation testbed with Hardware-in-the-Loop (HiL) capabilities. The system includes a multi-terminal medium-voltage (MVDC) and high-voltage direct current (HVDC) network weakly coupled to a network equivalent, represented by a scaled synchronous machine (SynM) to replicate grid inertia. Modular multilevel converters (MMCs) model the converters, while Power Hardware-in-the-Loop (PHiL) experiments integrate real power hardware. Dynamic interactions, including islanded conditions, are emulated to assess the performance of GFM controls and their interactions in HV/MV and AC/DC systems. The results demonstrate the compatibility of diverse GFM schemes with grid-following controls and synchronous machines, emphasizing their positive contributions to system stability. This modular demonstrator, as a realistic prototype of future power systems, provides a flexible platform for testing emerging GFM strategies and hardware, supporting the development of robust and stable inverter-based grids.

Keywords: grid-forming; grid-following; islanding; HVDC; MMC; MVDC multi-terminal; microgrid laboratory; real time; PHiL; phase-restoring principle; virtual synchronous machine

check for updates

Academic Editors: Dorin Petreus and Pedro J. Villegas

Received: 13 December 2024
Revised: 22 January 2025
Accepted: 8 February 2025
Published: 13 February 2025

Citation: Richter, M.; Kuri, A.; Richter, J.; Wagner, T.; Henninger, S.; Mehlmann, G. Demonstration of Grid-Forming Controls in Hybrid AC/DC Grid in a Real-Time PHiL Environment. *Electronics* **2025**, *14*, 730. https://doi.org/10.3390/electronics14040730

1. Introduction

The need for swift decarbonization is driving the rapid increase in renewable energy adoption. In particular, wind and solar power are expanding due to their widespread availability. However, integrating these intermittent renewables poses necessary requirements such as energy storage, new market models, and improved grid control. Traditionally, synchronous machines (SynMs) have provided stable voltage sources in power systems, but as more inverter-based generation is added, issues with conventional grid frequency and voltage control can arise. These problems are especially prevalent in island or weak power systems where the large grid impedance can lead to instability. This instability may stem from interactions between inverter phase-locked loops and current controllers and the characteristics of power systems with high levels of conventionally controlled wind, photovoltaic (PV), and battery energy-storage systems (BESSs) [1–4]. While mainland power systems may experience localized issues in areas with abundant PV and wind capacity, island power systems can face system-wide sub-synchronous control oscillations [5]. Similar challenges could potentially affect large interconnected power systems if inverter-based resources reach sufficiently high levels, since they have the primary control objective of injecting current into the grid. Their control stability relies on the grid to provide a strong voltage source, and hence they are referred to as grid-following (GFL) inverters.

Grid-forming (GFM) control is emerging as a pivotal solution to address dynamic challenges in weak power grids and to offer essential ancillary services. It represents an innovative frontier within modern power electronics, tailored to the needs of power systems increasingly characterized by a high penetration of renewables. These low inertia systems necessitate novel approaches. Current research on GFM inverters primarily focuses on developing advanced and effective control strategies, with comprehensive evaluations often conducted using offline simulation [6]. However, less attention has been given to larger, heterogeneous systems analyzed in the electromagnetic transient (EMT) domain. Investigating the interaction between different GFM inverters, GFL inverters, and SynMs is critical to understanding their performance in complex systems. According to [7–9], the main research directions in the field of GFM inverters are frequency and voltage control, as well as topics related to system strength. In the context of frequency control, it is particularly important to evaluate how effectively GFM inverters can regulate frequency in heterogeneous systems that also include GFL inverters and SynMs. The test system presented here incorporates such a heterogeneous setup, comprising two different types of GFM controls (VISMA, PRP), a grid equivalent with a scaled SynM, and GFL inverters. This configuration enables variation in system strength via the grid equivalent while also allowing for an analysis of the influence on the exciter of the SynMs. The newly developed GFM concept, called the Phase-Restoring Principle (PRP), represents a novel approach in this domain. Characterized by its PT1 behavior, global stability in inductive systems and limited vector shift, PRP has shown promise in small-scale studies [10,11]. A comparison of PRP with other GFM methodologies has yielded promising results [12]. However, it has not yet been tested in larger systems, making further research essential to evaluate its applicability and performance in complex and heterogeneous grid environments.

MVDC systems represent a new application for GFM control. In [13], it is suggested that a fast rollout of renewables such as wind in Northern Germany is facilitated by using $\pm$55 kV MVDC grids to collect the power from several wind farms and feed it in dedicated head station to the transmission grid. In order to enhance the stability of the connected AC system, a GFM control behavior is proposed instead of conventional GFL control, also incorporating BESSs on the DC side [14]. Due to the elimination of skin and proximity effects and reactive power losses associated with AC transmission, MVDC systems can significantly reduce transmission losses and extend the supply range due to lower voltage drops at the same power level [15]. Also, higher insulation-withstanding voltages and lower overvoltages in case of the DC operation of conventional AC transmission lines and cables allow for higher phase-to-ground RMS voltages, resulting in a significant increase in power transmission capacity and better utilization compared to AC operation [15–17].

The flexible-load flow control capability of DC systems enables the precise and optimized control of hybrid AC and DC systems. This allows DC technologies to support curative system operations through both load flow control and the provision of system services [18].

Reinforcing existing radial, open-loop distribution grids with MVDC, whether as back-to-back converters or DC links, can overcome operational limitations in integrating distributed generation. Additionally, it enhances operational flexibility, prevents AC fault propagation, and improves grid stability and voltage quality [19–21]. In other cases, it is advantageous to convert existing AC lines for DC operation, as in the project Angle DC [22], connecting the Isle of Anglesey with the mainland of North Wales.

These advantages make MVDC a valuable option for application areas such as distribution systems, rail systems, isolated shipboard systems, and offshore and onshore collection grids. Furthermore, there are suggestions to interconnect HV and MVDC systems through DC-DC converters in order to enable more power transfer flexibility [23].

To address all the aforementioned stability and conceptual challenges, this article demonstrates a future use-case scenario based on the MVDC system incorporating GFM control. The experiments presented here utilize real-time EMT simulations enhanced with a Power Hardware-in-the-Loop (PHiL) setup. This allows the dynamic interactions between the inverters and the power system to be observed without putting the real power system at risk. The ability to use real hardware reduces the reliance on computer model approximations and provides significantly more reliable insights into controller and equipment behavior [24–26]. Up to now, empirical field experiments and real-time simulations remain limited in this area, underscoring the need for the further exploration and validation of GFM concepts. In [27], investigations and performance comparisons are conducted for various prototype converters with GFM control using PHiL. The converters are appropriately scaled up and integrated into the IEEE 9-bus system to examine frequency stability in a low-inertia system. In [28], it is demonstrated how PV and battery converters can be designed for a microgrid using PHiL. The combination of renewable resources and GFM storage systems to so-called hybrid power plants is becoming increasingly important to provide inertia. The study in [29] builds upon [28] by validating a GFM hybrid power plant, consisting of a 430 kW PV system and a 1 MW battery with centralized park control, using PHiL. An important contribution is made in [30], which investigates a GFM PV inverter in the MW range within a large and realistic real-time power system model of Maui island. This work provides practical evidence that GFM inverters can stabilize the grid and highlights their real-world applicability. Unlike typical PHiL setups, which are often confined to smaller power ranges and small-scale power system models, this study validates GFM behavior at a much larger scale. The paper presented here follows a slightly different approach: rather than focusing on performance comparisons of various control schemes, the emphasis is placed on the systemic interaction of different GFM controls with GFL inverters and SynMs. This is investigated using a hybrid AC/DC test system and aligns with the research goals identified in [7–9] to extend studies to heterogeneous systems. Control-Hardware-in-the-Loop (CHiL) and PHiL studies have additional significance in the light of various national efforts of GFM in bulk power grids. The integration of GFM into bulk power systems will proceed gradually with the demonstration of key functionalities of this technology [8]. The plans outlined in the System Stability Roadmap by the German government are particularly ambitious, aiming to gain substantial experience with GFM by 2027 and making GFM a key contributor to provide system stability in Germany by 2030 [31]. According to [24,32], real-time simulation-based testing is highly suitable both in the implementation and prototyping phases as well as during the rollout phase of new technologies. HiL is therefore an ideal tool to gain the necessary experience with this technology and serves as a de-risking measure before the widespread integration of GFM inverters in bulk power systems.

This experimental result represents a significant step towards ensuring the system stability of converter-dominated power systems, in particular HVDC or MVDC, PVs, wind generation, and BESSs. The work describes the main motivation for such a demonstration, providing an accurate analysis of the technical characteristics. It also proposes a detailed description of each installation and the results obtained or expected. The responses of the demonstrators are evaluated, marking their analogies and differences of the control concepts, trying to chart the development trajectory of these new technologies to the power system, and suggesting some future developments for experimental tests on pilot systems.

The structure of this article is as follows. Section 2 describes the hybrid HVDC/MVDC test bench and associated details. Section 3 provides insights into the design and control implementation of the GFL converters and DC-DC converters. The utilized and incorporated GFM control schemes are described and discussed in Section 4. Section 5 analyzes the complete test setup under various futuristic and challenging scenarios. The demonstration of the overall setup, its capabilities, and the results provided are discussed. Based on the outcome of the work, Section 6 provides a thorough discussion of the methodology and approach, addressing limitations and offering a reflective analysis. Additionally, it outlines future topics that merit further exploration. Finally, Section 7 concludes the work.

2. Hybrid HVDC/MVDC Test Bench

The simulation and hardware test bench setup are presented in this section, which describes the hybrid HVDC/MVDC test bench with the integrated GFM controls and its interconnection to the Microgrid-Laboratory. An overview of the system topology is given in Section 2.1, followed by a description of the modeled DC-DC converters in Section 2.2 and the basic design of the modeled MVDC MMC converters, used as head stations, in Section 2.3. In Section 2.4, the multi-terminal (MT) control of the HVDC/MVDC test bench is briefly described. At last, in Section 2.5, the interconnected Microgrid-Laboratory is presented.

2.1. System Topology

The MVDC/HVDC test system presented here is an essential part of a larger real-time test platform, the so-called Kopernikus ENSURE Co-Demonstration Platform [33]. This platform enables the integration of the MVDC/HVDC test system, or parts of it, into power system models based on real-life data, such as ENTSO-E TYNDP or Day-Ahead Congestion Forecasts data. Additionally, distributed real-time simulation via VILLASnode [34] allows for coupling different laboratories for joint simulations. The following investigations focus exclusively on the actual MVDC/HVDC test system to study the interaction of the various control systems. However, reference is made to [35], where part of the test system has been integrated into a larger transmission system model of Northern Germany.

Figure 1 displays the hybrid HVDC/MVDC test bench. The main parts of the test system are a Microgrid-Lab (see Section 2.5), a simulated dynamic PV plant, loads, and a MTDC system consisting of a MVDC and HVDC. Both DC systems are designed as cable based symmetrical monopoles and are operated at ±320 kV (HV) and ±55 kV (MV). An interconnection with a MV/HV DC-DC converter allows for power exchange between the voltage levels. In addition, a BESS is connected centrally into the MVDC using an MV/MV DC-DC converter. Both DC-DC converters are described in Section 2.2. MT operation is possible with droop control described in Section 2.4. The HVDC system is interconnected with 320 kV XLPE cables with parameters derived from [36]. For the interconnection of the MVDC system, the concept of using conventional 20 kV MVAC cables for DC operation is adopted from [13], the feasibility of which is based on research of [37–40]. Related studies have demonstrated that commercial 12/20 kV XLPE AC cables can be utilized for DC operation at voltage levels of up to ±55 kV. As stated in [37], the DC power transmission capacity is determined using (1).

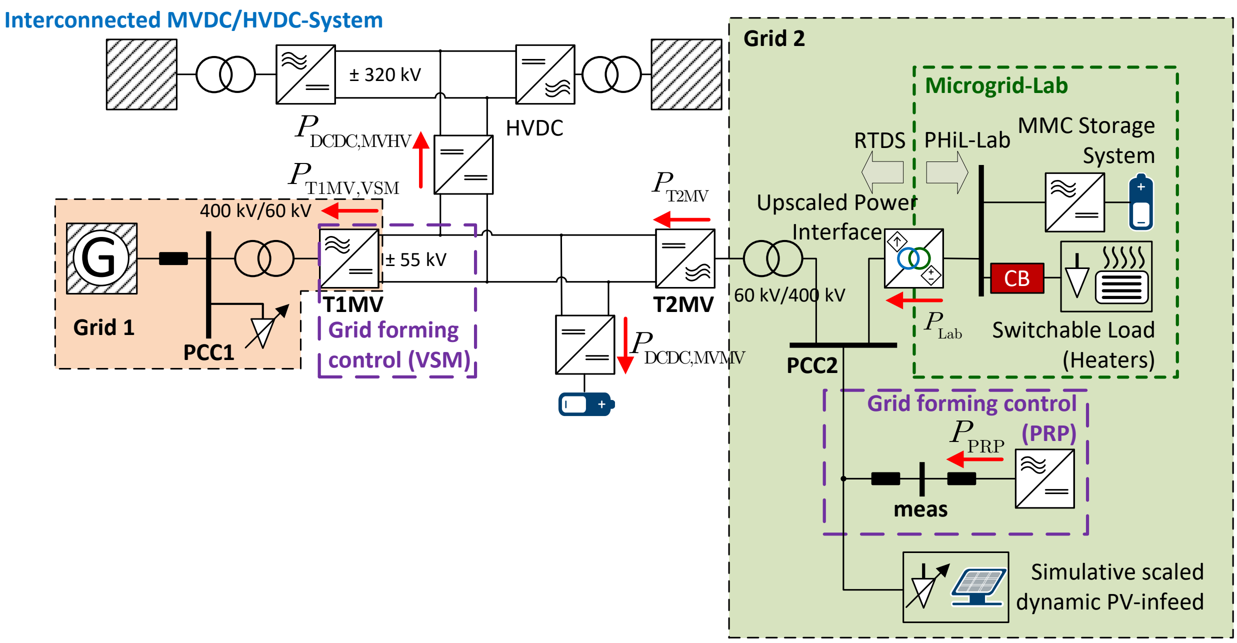

Figure 1. MVDC-HVDC test system.

$$\frac{P_{DC}}{P_{AC}} = \frac{m \cdot U_{DC} \cdot I_{DC}}{\sqrt{3} \cdot U_{AC} \cdot I_{AC} \cdot \cos \Phi} \tag{1}$$

For bipolar operation ($m = 2$), with $I_{DC} = I_{AC}$, $U_{DC} = \pm 55$ kV and U_{AC} = 20 kV, a significantly higher DC power transmission capacity—approximately 350%—can be calculated for typical values of $\cos \Phi$ between 0.85 and 0.95 [37,38]. In the test bench, three parallel XLPE cables of type 1 × 240/25 are used for each pole, resulting in a power transport capacity of 150 MW. An overview of all cable data is presented in Tables 1 and 2.

Table 1. Cable parameters for HVDC cable (based on Submarine XLPE HVDC cable [41]).

Layer/Material	Radial Thickness (mm)	Resistivity ρ (Ωm)	Relative Permittivity ϵ_r	Relative Permeability μ_r
Core (Copper)	24.9	2.2×10^{-8}	1	1
Screen (Semi-cond. polymer)	1	-	-	-
Insulation (XLPE)	18	-	2.5	1
Screen (Semi-cond. polymer)	1	-	-	-
Sheath (Lead)	3	2.2×10^{-7}	1	1
Inner Jacket (Polyethylene)	5	-	2.3	1
Armour (Steel)	5	1.8×10^{-7}	1	10
Outer Cover (Polypropylene)	4	-	1.5	1

Table 2. Cable parameters for MVDC cable (based on MVAC cable NKT NA2XSY 12/20 [42]).

Layer/Material	Radial Thickness (mm)	Resistivity ρ (Ωm)	Relative Permittivity ϵ_r	Relative Permeability μ_r
Core (Aluminum)	9.05	2.82×10^{-8}	1	1
Screen (Semi-cond. polymer)	0.3 *	-	-	-
Insulation (XLPE)	5.5	-	2.3	1
Screen (Semi-cond. polymer)	0.3 *	-	-	-
Screen (Copper)	1.85	1.68×10^{-8}	1	1
Sheath (Polyvinyl chloride)	2.5	-	8	1

* Thickness of semi-conductive screen taken from N2XS2Y of [43].

The focus of the investigation presented in this paper are two different GFM control schemes and their interoperability via the MVDC system. The Microgrid-Lab (dotted green in Figure 1) is linked to the real-time simulation model via a linear power amplifier, at the star point of common coupling (PCC2) of AC Grid 2 on the right side. The Phase-Restoring Principle (PRP)-based GFM control scheme (see Section 4.1) is implemented at a converter source with sufficient headroom via a coupling transformer. The PRP and the simulated aggregated dynamic PV are also connected to PCC2.

As described in Section 4.3, an MVDC converter terminal that includes the GFM scheme based on VSM is integrated via a coupling transformer at the node named PCC1 and has a power rating of ±100 MW, and $Q = \pm 30$ MVAr.

The test bench also includes Thévenin equivalents as external grids connected to the HVDC terminals. In AC Grid 1, however, a rotating grid equivalent with typical generator controls is chosen to demonstrate the grid forming and supporting capabilities of the VSM control of the MVDC terminal T1MV. The grid parameters of the grid equivalent are listed in Table 3. The controllers IEEEG1, EXST1, and IEE2ST are designed according to [44–46].

Table 3. Parameters of the rotating-grid equivalent—AC Grid 1.

Parameter	Value
$S_{\text{gen,r}}$	1220 MW
$U_{\text{AC,r}}$	15/400 kV
H	4.7 s
S''_{k}	3.18 GVA
Govenor type	IEEEG1
Excitor type	EXST1
PSS type	IEE2ST

The HVDC terminals are based on the MMC topology and its design parameters are based on the Inelfe project [36]. For high-power converters used in high and medium voltages, the MMC topology is the state-of-the-art converter type. To the authors' knowledge, no design parameters for MMCs with a DC side voltage of 110 kV have been published yet. Therefore, a basic design of the MV MMC is carried out based on HV MMC as described in Section 2.3.

The common time step, which is also applied in this work, is 50 µs, but the power electronic components (e.g., converters) are implemented in substep with a time step of 5 µs.

2.2. HVDC/MVDC Interconnection and Battery Storage Integration via DC-DC Converters

The coupling converter, connecting the MVDC and HVDC grid, is based on [47]. As the topology, an isolated MMC DAB with front-to-front configuration is chosen as depicted in Figure 2. The design parameters are derived from [47], specified in Table 4, with a rated power of 200 MW and a frequency of 150 Hz at the front-to-front AC link.

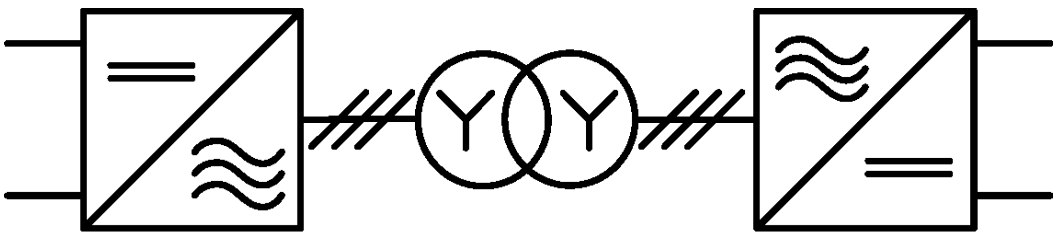

Figure 2. Dual-active-bridge DC-DC converter with front-to-front MMC topology.

Table 4. Design parameters of MV/HV DC-DC Converter.

Parameter	Value
P_r	200 MW
$U_{DC,HV}$	640 kV
$U_{DC,MV}$	110 kV
f_{AC}	150 Hz
$U_{AC,HV}$	377 kV
$U_{AC,MV}$	56 kV
$U_{SM,HV}$	2.0 kV
$C_{SM,HV}$	0.93 mF
$n_{SM,HV}$	330
$U_{SM,MV}$	2.0 kV
$C_{SM,MV}$	6.8 mF
$n_{SM,MV}$	51

For the BESS, a power rating of 55 MW is chosen and connected to the MVDC grid via a multilevel three-phase dual-active-bridge (3p-DAB) converter. Its original design is derived from [48] and slightly modified by lowering the secondary output voltage at the battery rack connection point from the original 5 kV to 1 kV.

For the multilevel 3p-DAB converter, an input-series-output-parallel (ISOP) configuration, as depicted in Figure 3, is used, which consists of n_{SM} submodules (SM) connected in series on the primary and in parallel on the secondary side. To achieve a total power of 55 MW, the parallel connection of 10 converters with associated battery racks, each with an individual power of 5.5 MW, is assumed. The design parameters are listed in Table 5.

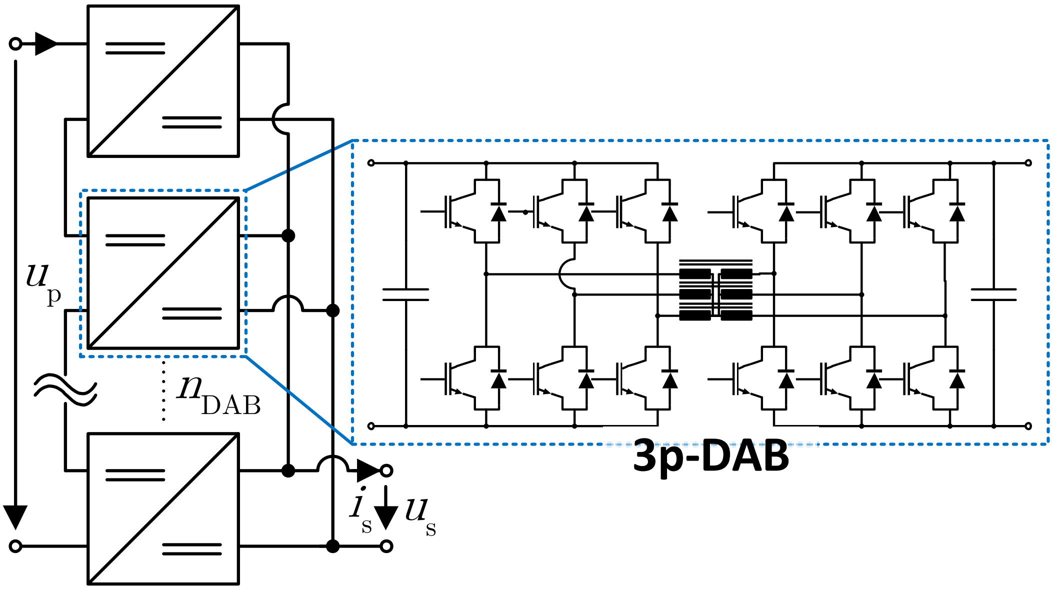

Figure 3. 3p-DAB series-input-parallel-output multilevel DC-DC converter.

Table 5. Design parameters of MV/MV DC-DC converter with BESS.

Parameter	Value
$P_{r,tot}$	55 MW
$P_{r,DAB3-SM}$	250 kW
$U_{pri,DC}$	110 kV
$U_{sec,DC}$	1 kV
f_s	1 kHz
L_σ	3.7 mH
$n_{DAB3-SM,per\ ISOP}$	22
$n_{ISOP-conv\ in\ parallel}$	10

To reduce computational power, the 3p-DAB is modeled with the least detailed modeling type, the state-space averaging approach, as applied in [48–50].

2.3. Basic Design of MVDC MMC

The basic design for the MVDC MMC is derived from MMC design parameters of the HVDC project [36], under certain assumptions. The resulting design parameters for the HVDC and MVDC MMC terminals are listed in Table 6. A rated power for one converter terminal of 105 MVA with an operating range of ±100 MW and ±30 MVar is chosen. Moreover, nominal voltage variations in the range of 0.90–1.1 pu at the AC side and 0.95–1.05 pu at the DC side are considered. The MVDC terminal shall be connected to the high voltage grid. Based on typical transformer short-circuit impedances and no-load losses, given for different rated power ranges in [51], the coupling transformer is parametrized for a rated power of 105 MVA. The primary grid-side voltage is 400 kV, which is the typical transmission grid voltage in Germany. The secondary converter side voltage is 60 kV. This voltage guarantees that for all nominal AC and DC side voltages and power ranges an amplitude modulation index below $2/\sqrt{3} \approx 1.15$ is fulfilled. This is the maximum admissible value for the control voltage of a converter arm in case of a half-bridge-based MMC, taking into account a third harmonic injection.

Table 6. Design parameters of HVDC and MVDC MMC terminals.

	MVDC	HVDC
$S_{r,MVDC}$	105 MVA	1000 MVA
$U_{g,AC,HV}$	400 kV	400 kV
$U_{c,AC,HV}$	60 kV	333 kV
$U_{DC,pn}$	110 kV	640 kV
n_{SM}	59	280
u_{SM}	2.3 kV	2.3 kV
C_{SM}	4.2 mF	8.5 mF
$L_{arm,MVDC}$	8.6 mH	50 mH
$R_{arm,MVDC}$	0.504 Ω	1.57 Ω

Further, a rated SM voltage of 2.3 kV is selected for both the HVDC and MVDC MMC, with the use of 4.5 kV HV-IGBTs as deployed in HVDC projects of Siemens AG [52]. To derive the necessary SM number per arm, the maximum necessary control voltage of the converter in the presumed operating range and a SM redundancy of 10% is taken into account. Additionally, to determine the required SM capacitor size, the power and current equations, given in detail in [53], are applied and evaluated. The arm reactors connected in series to the SMs in each converter arm are designed on the premise of limiting the rise in current for a certain delay time of fault detection, and scaled for the MVDC system voltage based on [47]. Since there is no grounding on the DC side in a symmetrical monopole, a ground reference is introduced on the AC side using a star-point reactor.

2.4. DC-System Control

In principle, the power and voltage control in DC systems can be handled with different DC controls, as the singular DC voltage control, formerly known as master–slave control (controversial terminology), the voltage margin, and the voltage droop control [54]. For multi-terminal systems, however, the voltage droop control offers the most flexibility and smoothest voltage-stabilizing effect. The droop control handles the voltage and power control in a distributed way by assigning multiple converter stations a linear DC voltage-dependent $P_{DC}(U_{DC})$ setpoint curve. The implemented power droop control is depicted in Figure 4. In the event of unforeseen outages and failures of converter stations or power plants feeding into the DC system, or to cope with simple power fluctuations, each droop-controlled station participates in stabilizing the DC voltage by adjusting its power setpoint.

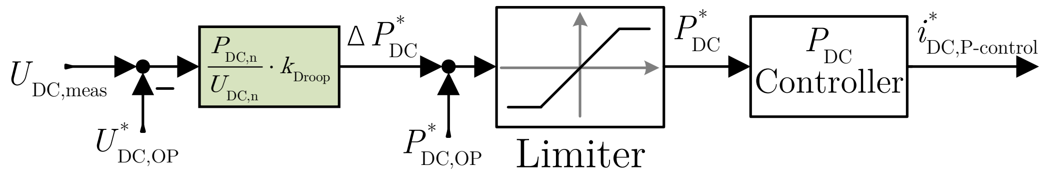

Figure 4. Power droop control for the voltage control of the HV and MV MTDC system.

In the implemented MVDC/HVDC test bench the station T2MV, both DC-DC converters and both HVDC stations are equipped with droop controls with parametrizable droop constants.

2.5. Real-Time Simulation and Low-Voltage Laboratory

The Low-Voltage Microgrid Laboratory (LV-Lab) is interfaced to the hybrid HVDC/MVDC test bench, which is implemented on digital real-time simulators within the Real-Time Simulation Laboratory. The LV-Lab integrates real power equipment, such as battery storages, renewable energies, and loads, in combination with power amplifiers for PHiL simulation to achieve a flexible and realistic testbed for the investigation of sustainable energy supply. A scheme of both connected laboratories is depicted in Figure 5. Xilinx's aurora protocol-based communication via fiber-optical cables connects the RTDS NovaCor Simulator of the Real-Time Simulation Laboratory with power amplifiers within the Microgrid-Lab.

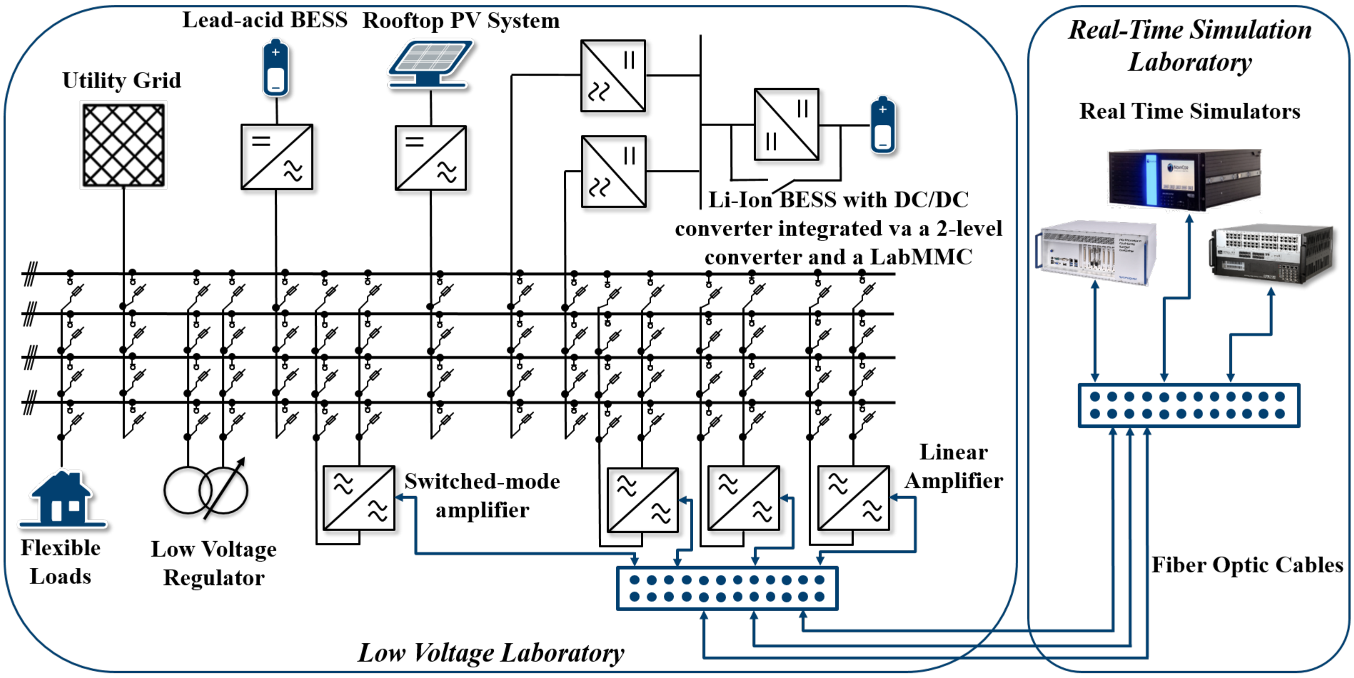

Figure 5. Connection between Real-Time Simulation and Low-Voltage Laboratory.

A NovaCor Chassis from RTDS is utilized for the test bench. Three fiber-optical cables connect the real-time simulator and a linear power amplifier (LPA). For the tests, a Spitzenberger&Spies amplifier with one APS5000 system per phase is used (represented by one linear amplifier in Figure 5). This allows for a four-quadrant-rated power provision or consumption up to 5 kVA per phase. The tests are performed with the amplifier in voltage control mode with current limits. An enhanced ideal transformer method [55] acts as the interface between the HV simulation and the LV-Lab. The scaling factor for the feedback current and thus the power of the connected hardware is set to 1000 to match the dimensioning of the simulated components. The real-time simulator sends voltage signals at a selected connection point and transfers the signals to the power amplifier. The power amplifier sets an output voltage, which leads to a current flow with connected hardware. The current is measured within the power amplifier and transferred back to the real-time simulator by means of a current injection at the interconnection point. Different static and dynamic power hardware of the Microgrid-Lab is interfaced with the HVDC/MVDC test bench. These include a purely resistive three-phase heating load with a total loading of up to 7 kW and a lithium-ion battery. The storage system is integrated parallel via a 2-level converter and a laboratory-scale modular multilevel converter (LabMMC) (see Figure 5), in which various GFL and GFM control schemes are implemented. These include setpoint operation, various droop controls, and virtual inertia provision [56]. In the context of this paper, only the LabMMC is considered, since 2-level converters inherently induce more non-idealities, which subsequently are also scaled with the used interfacing method [55] and thus would produce unrealistic load behavior in high-voltage applications, which is the primary goal of this integration. The LabMMC has four half-bridge submodules per converter arm. The rated apparent power of the LabMMC is 25 kVA [57]. This work considers the LabMMC in setpoint operation as a variable GFL load. The described lab setup is depicted in Figure 6, including the LPA (a), the resistive load (b), and the LabMMC (c).

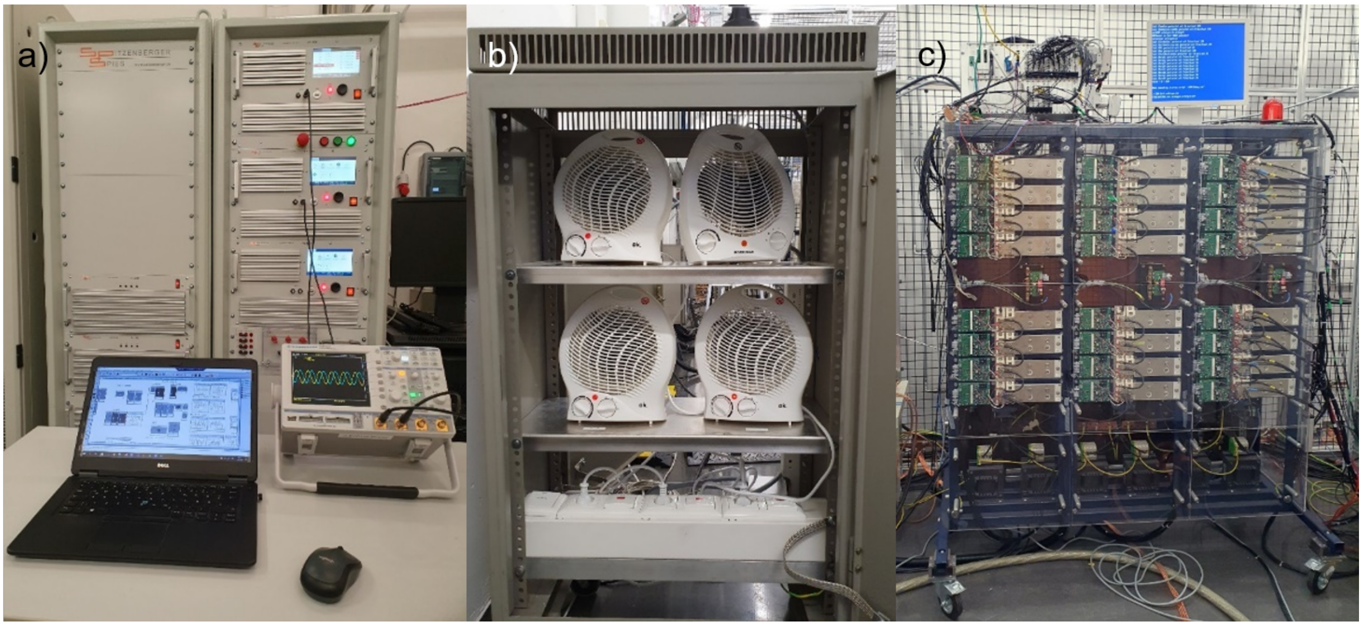

Figure 6. Connected hardware during PHiL-coupling: (**a**) power amplifier, (**b**) three-phase resistive load, (**c**) LabMMC connected to the Li-ion storage.

Additionally, a virtual scaled and compressed photovoltaic plant based on the data of the rooftop 17 kWp PV system is simulated in real-time simulation to ensure reproducibility and dynamic behavior. The data are collected from three strings with east, south, and west orientation, with two module types installed with a peak power of 285 Wp and 295 Wp, respectively. The strings are connected to the LV-Lab via two different SMA inverters with a rated power of 7 kVA and 9 kVA.

3. Control Design of Grid-Following Converters and DC-DC Converters

3.1. Control of Grid-Following MMCs

The converter head stations of the HVDC link and the head station T2MV are operated as grid-following converters coupled to the DC systems with a DC voltage-stabilizing $P_{\mathrm{DC}}(U_{\mathrm{DC}})$ droop control. The control scheme, depicted in Figure 7, is set up as a cascade control. In the upper level, it comprises the DC power droop control and controllers for total, horizontal, and vertical balancing. Since the DC power is specified by the droop control, the total energy balancing is performed via the AC grid. The grid current control is a vector current control operating in positive and negative sequence. The energy-balancing controllers provide setpoints for the circulating-current control. The current controllers then provide reference voltage components. The control of the GFL converters is described in [58].

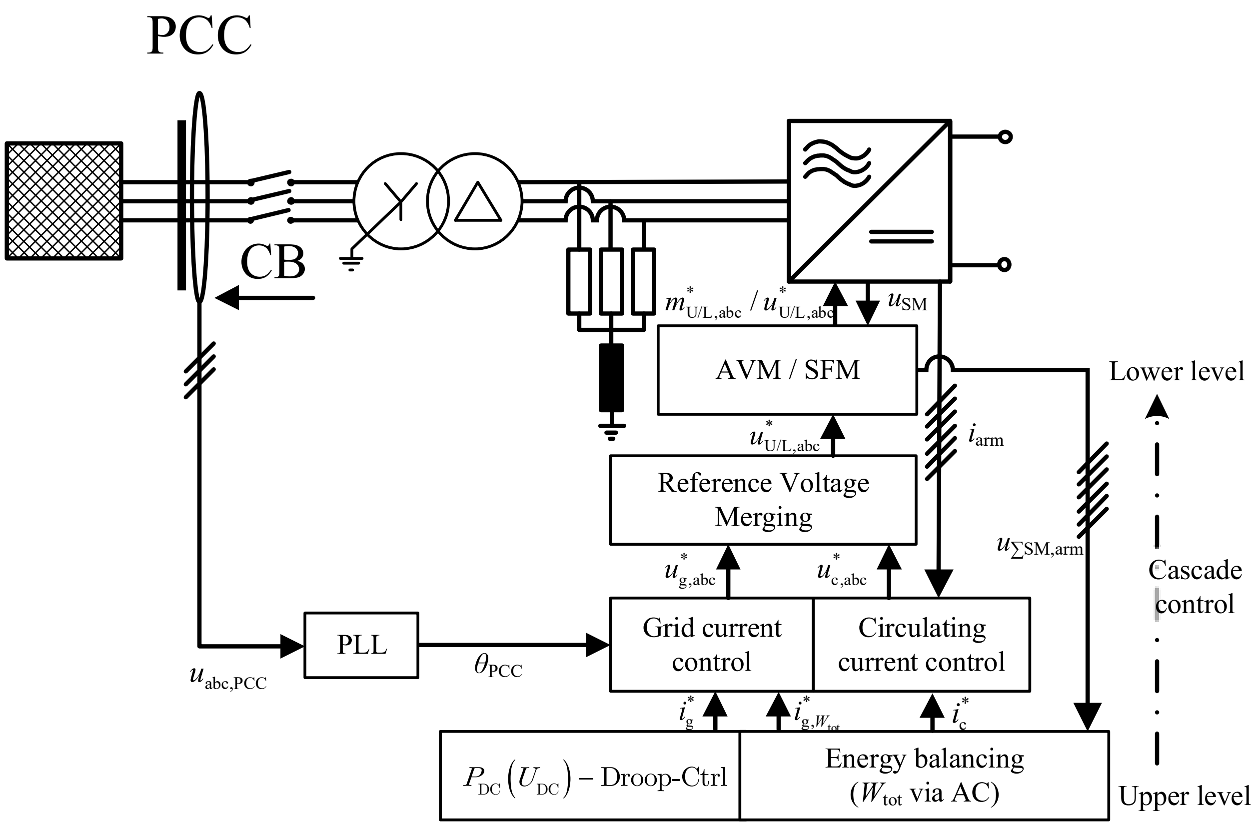

Figure 7. Hierarchical MMC control structure for grid-following operation.

3.2. Control of MV/HV DC-DC Converter

The MV/HV DC-DC converter, linking the MVDC and HVDC systems, is formed by connecting two MMCs at their AC side with a three-phase connection transformer, which is necessary to step-up the voltage. The advantage of this configuration is that certain control concepts, such as the vector current control and energy balancing within the converters, can be adopted from conventional MMC converter control used in the head stations in the HVDC systems. The control scheme of the MV/HV DC-DC converter is depicted in Figure 8. The design parameters of the MVDC/HVDC DC-DC converter are listed in Table 4.

On the HV side of the AC link, the three-phase AC voltages are specified with rated values and are used as synchronization references for the AC vector current control of the counterpart MV MMC. Due to the necessity of power balance between both DC and AC sides in a steady state, the power transfer of the DC-DC converter can be specified only on one DC-side. In this setup, the DC power transfer is set on the MVDC side and determined by a static power setpoint, together with a dynamic adaptation by means of a voltage-dependent $P_{DC}(U_{DC})$ droop control to take part in the voltage stabilization of the MVDC grid. To balance the energy of both MMC converters, the total energy balancing of the MVDC MMC is performed via the AC side, calculating a feed-forward signal for the AC current $i^*_{d,W_{tot}}$ and a feed-forward current for the DC side of the HVDC-side MMC $i^*_{DC-HV,ff,P_{DC}}$. The total energy of the HVDC MMC, on the other hand, is balanced via the DC side to allow for a smooth power transfer in the direction MVDC → MV/HV-AC → HVDC.

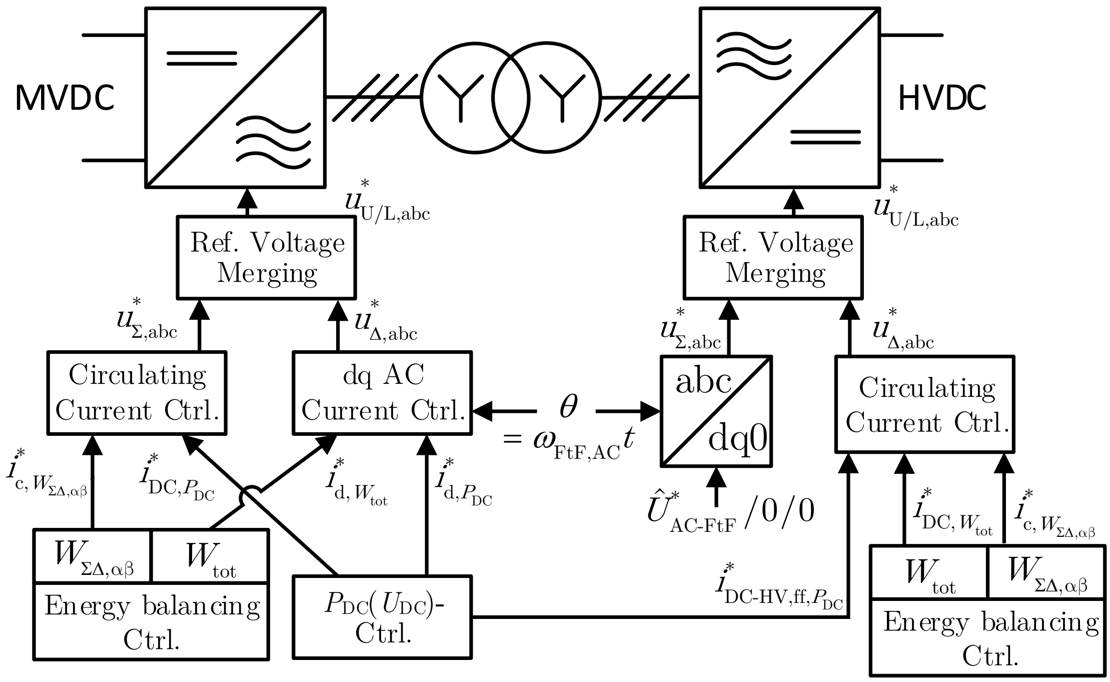

Figure 8. Control structure of DC-DC-converter for the coupling of the MVDC and HVDC system.

3.3. Control of MV/MV DC-DC Converter of BESS

The control of the MV/MV DC-DC 3p-DAB SIPO (Serial Input, Parallel Output) converter, interconnecting the BESS and MVDC system, consists of two cascaded stages as depicted in Figure 9. In the upper layer, a $P_{DC}(U_{DC})$ droop control is implemented providing a DC voltage-dependent power setpoint with an offset value as the operational setpoint.

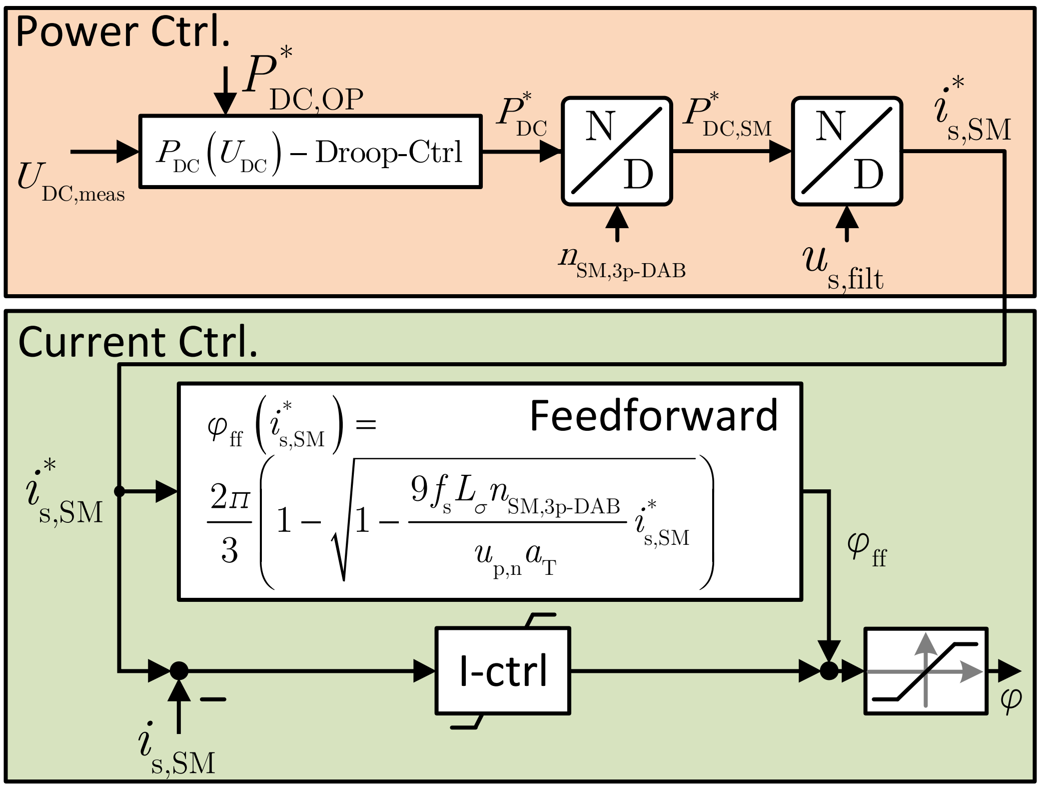

Figure 9. Control structure of MV/MV DC-DC converter based on 3p-DAB SIPO topology.

Due to the cascaded structure of the SIPO converter, each SM would have its own current control and the series connection of the SMs would require an additional balancing control scheme in real applications, as suggested in [59]. For the 3p-DAB SIPO configuration in this test bench, however, an average-value model representation of the SMs is assumed. This implies that the SMs are ideally balanced, allowing for a single current control to be applied across all DAB SMs. The power setpoint is translated into a DC current setpoint for the secondary side of the DAB SM. The current control employs the phase-shift angle ϕ, which serves as the control signal, introducing a delay for the control impulses on the secondary side, resulting in a corresponding delay of the controlled voltage relative to the primary side. The lower-level current control uses the phase-shift angle ϕ as the control signal, relying on the electrical steady-state relationships outlined in (2) and (3). They describe how the secondary output current $i_{\mathrm{s,SM}}$ and the resulting secondary-side DC power of one 3p-DAB SM depend on the primary and secondary SM voltages $u_{\mathrm{p,SM}}/u_{\mathrm{s,SM}}$ and the phase-shift angle ϕ. The control consists of a feed-forward term and a supplementary integral controller.

$$i_{\mathrm{s,SM}} = \frac{u_{\mathrm{p,SM}}}{\omega L_{\sigma}} \left(\frac{2}{3} - \frac{\phi}{2\pi} \right) \tag{2}$$

$$P_{\mathrm{SM}} = u_{\mathrm{s,SM}} i_{\mathrm{s,SM}} = \frac{u_{\mathrm{s,SM}} u_{\mathrm{p,SM}}}{\omega L_{\sigma}} \left(\frac{2}{3} - \frac{\phi}{2\pi} \right) \tag{3}$$

4. Grid-Forming Control Schemes

4.1. Phase-Restoring Principle

A novel control scheme called the Phase-Restoring Principle (PRP) is utilized. This control scheme inherently achieves the post-disturbance operating point directly and thus forms the grid. Figure 10 shows the block diagram of the controller. The control scheme allows for nominal frequency to be restored following a disturbance by fixing the measurement node voltage. Thus, the scheme provides the power system with an equivalent qualitative response of a SynM with large inertia. The control scheme is not based on a phase-synchronized coordinate system; rather, it transforms the phase to participate in the power exchange caused by a disturbance. Hence, it rotates in the direction opposite to the standard dq frame, as displayed in the phasor diagram of Figure 11.

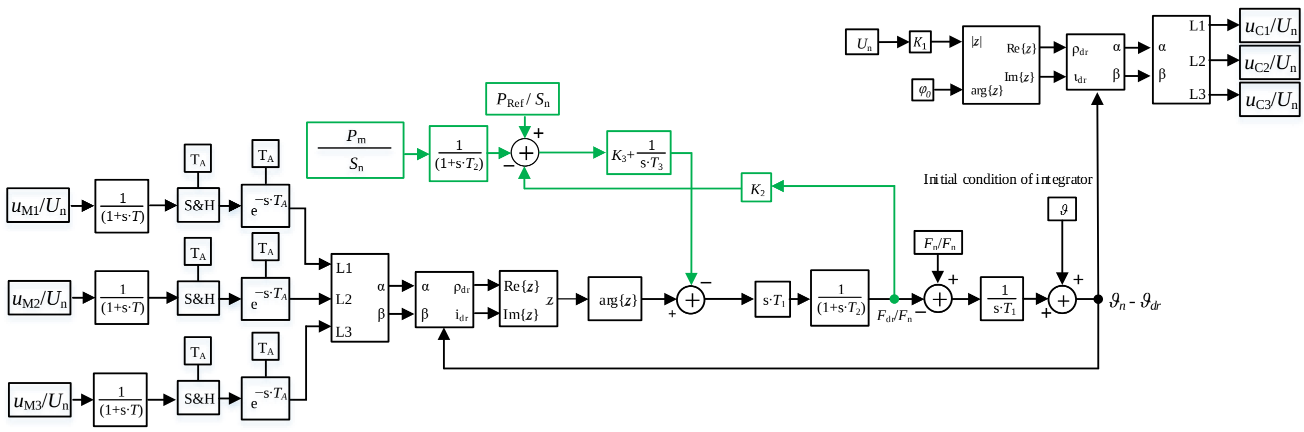

Figure 10. Block diagram of phase-restoring control scheme with active power control for grid-forming converter control [11].

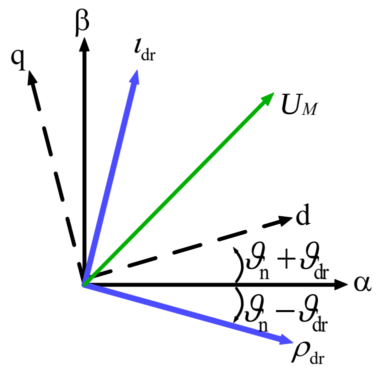

Figure 11. A phasor diagram interpretation of the phase drift ϑ_{dr} in $\alpha\beta$ frame. The green line represents an arbitrary measured voltage, dashed lines represent the fixed dq frame, and the blue lines represent the new co-ordinate $\rho_{dr}\iota_{dr}$ due to the frequency drift [10,11].

This control achieves initial synchronization by setting the converter voltage phase to the measured voltage phase at control release. It continuously transforms the measured voltage phase into a new reference frame, ρ_{dr} ι_{dr}, and in the direction of the prospective future stable operating point, thereby adjusting the output phase of the converter and fixing the phase of the measured voltage. The frequency is contained in the control loop and manifests at the systems' steady state. Adding an active power-control loop responsible for setpoint changes and power-dispatch capacity enhances the control concept. PRP with the active power control displays a first-order system response as opposed to the second-order swing equations of the synchronous machine. The addition of the active power-control loop helps ease the constant frequency output of the control.

PRP is the lowest building block and is entirely GFM. The slower control dynamics are built over it. It inherently prioritizes response to disturbances over setpoint changes and limits vector shifts, as required by services mentioned in the NERC and UK Grid Codes [60,61]. Enhanced PRP with active power control is compatible with other sources in the power system as a GFM requirement, mentioned in [62]. It displays three essential aspects of GFM control requirements mentioned by various grid codes—voltage source characteristic, priority of disturbances, and active power control. Furthermore, the concept offers global stability with a suitable choice of parameters. Further details on this work are available in publications [10–12]. This concept is implemented in the real-time simulation test bench to demonstrate its GFM capabilities with other sources, control interaction, and attaining stability in a converter-dominated network. Furthermore, the response with PHiL is investigated.

4.2. Power-Forwarding Control

In Grid 2, the PRP-controlled converter is the only grid-forming converter and is without further measures, compensating all power fluctuations introduced through the simulated RES infeed, with the load steps performed at the Microgrid-Lab or in case of power adaptations transferred through T2MV. Depending on the power changes, the PRP converter could reach its operating limits unless additional measures are taken to partially balance the connected components. Therefore, an additional slow control, referred to here as the power-forwarding control, is added. It is a kind of slow secondary control, which dynamically adapts the power setpoints of terminal T2MV of the BESS system, as well as the terminal T1MV, with the aim to relieve the PRP converter and increase its available power range for incoming power imbalances in Grid 2. The control scheme is depicted in Figure 12. It consists of two low-pass filters with different time constants; the upper one has a larger cutoff frequency f_{c1} than the lower one, with lower cutoff frequency f_{c2}. The measured power of the PRP-controlled converter is fed as input to the filters. The task of the slower filter path is to retrieve the base loading of the PRP converter, and the upper filter path will only filter out fast power spikes. A sample-and-hold block makes it possible to freeze the current base loading at a given time point after the ramp up of the system. Changes in the power output from this base loading are then forwarded as setpoint adaptations to the other converters to change the load flow and relieve the PRP. A switch allows the power to be routed through T2MV to the BESS or to the other head-station T1MV. If the sample-and-hold block is not activated, both filters will act as a band-pass filter and forward power fluctuations in a certain frequency range.

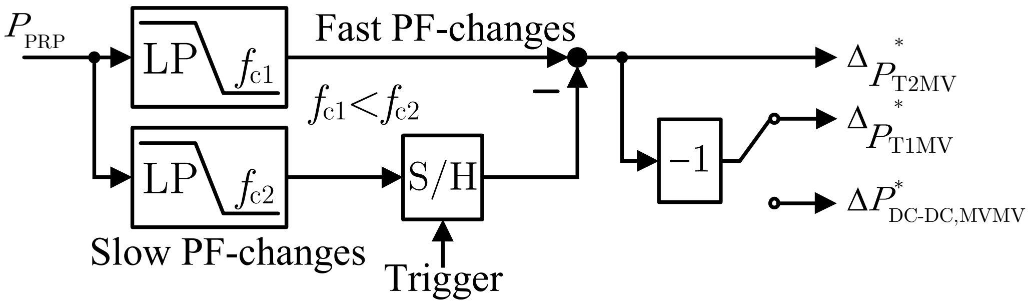

Figure 12. Power-forwarding control structure for relief of the grid-forming PRP converter.

4.3. Control of Grid-Forming VSM MMC

The head-station T1MV is operated as GFM converter, adopting the VSM control scheme described in detail in [63,64].

The VSM-based GFM control, depicted in Figure 13, is organized as cascaded control with the VSM and energy-balancing control at the upper level followed by a circulating-current control on the lower level. The VSM control forms the upper-level AC control part, where the relative phase angle of the VSM and its amplitude in relation to the voltage at the connection point determines the active and reactive power exchanged. This part replaces the active/reactive power and AC-grid current control used for the traditional grid-feeding MMC control. The total energy balancing is realized via the DC side to keep the total energy of MMC and its SMs balanced.

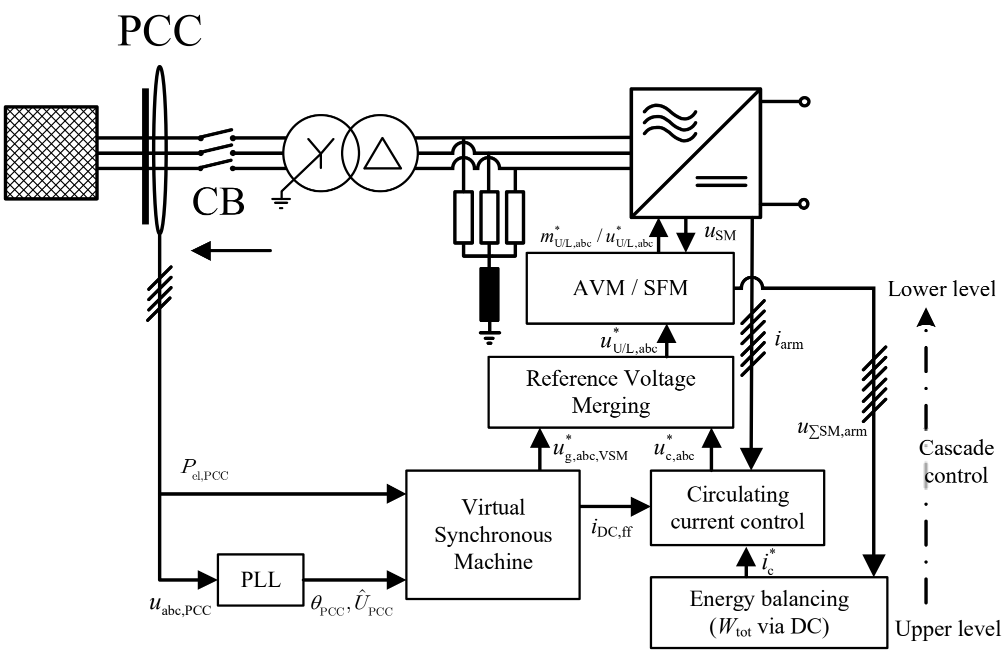

Figure 13. Hierarchical MMC control structure for VSM operation.

Further, it has proven useful in the case of transients in the AC grid, leading to fast AC power output changes, to introduce an additional feed-forward DC current $i_{\mathrm{DC,ff}}$, which is calculated on basis of the measured and filtered AC power and AC/DC voltages.

In this VSM-controlled MMC, the circulating-current control is the only current control implemented, to control the DC side and internal circulating currents. Both the VSM control and circulating-current control provide reference voltage components, which are merged and forwarded to the modulators of the converter arms.

The implemented VSM control structure is depicted in Figure 14 and is based on the reduced second-order differential equation of motion of a SynM given in (4) and (5).

$$J_{\mathrm{VSM}} \cdot \ddot{\theta}_{\mathrm{VSM}} = T_{\mathrm{m}} - T_{\mathrm{el}} - K_{\mathrm{d}} \cdot \dot{\theta}_{\mathrm{VSM}} \tag{4}$$

$$\dot{\theta}_{\mathrm{VSM}} = \omega_{\mathrm{VSM}} \tag{5}$$

T_{m} stands for the mechanical torque, T_{el} for the electromagnetic torque, and K_{d} and J_{VSM} for the parametrizable damping factor and virtual inertia constant, respectively. The normalized values used for the further investigations are $H_{\mathrm{VSM}} = 10\,\mathrm{s}$ and $K_{\mathrm{d,pu}} = 120\,\mathrm{pu}$, based on $S_{\mathrm{VSM,r}} = 100\,\mathrm{MVA}$ and $f_{\mathrm{n}} = 50\,\mathrm{Hz}$. T_{el} represents the torque introduced by the power exchange with the AC grid and is determined by the division of the measured power at the PCC with the current internal mechanical speed ω_{VSM}. In the case of an increased power exchange in the direction of the AC grid, the virtual machine is decelerated, or in the case of a power reduction, it is accelerated. Since no real mechanical drive system and power plant is involved, the mechanical torque T_{m} is only a virtual signal, which can be used to change the power setpoint P_{m} of the VSM. It is derived by the division of the power setpoint with the current internal mechanical speed.

The reference voltage of the VSM, which represents the synchronous internal voltage, is calculated with a rotation matrix using the internal machine angle θ_{VSM} and the virtual excitation amplitude $\hat{U}_{\mathrm{VSM}}$.

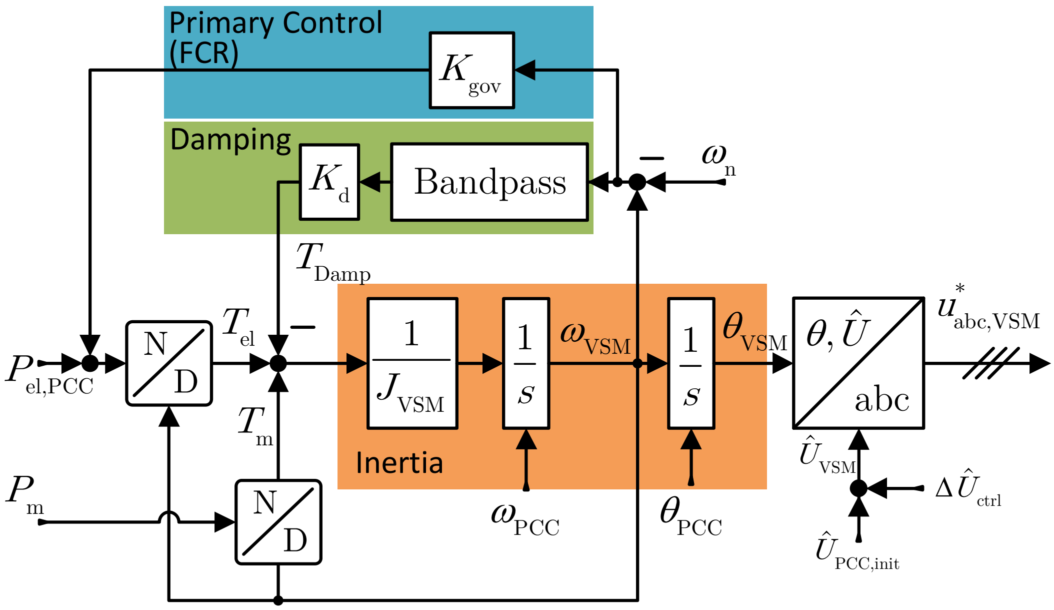

Figure 14. Control structure of virtual synchronous machine.

To prevent high reactive power exchanges with the external grid, the excitation value should be aligned to the grid voltage when connecting the converter. Thus, it is initialized with the measured voltage amplitude $\hat{U}_{\mathrm{PCC}}$ at the PCC during the synchronization procedure. Further, both integrators are initialized with θ_{PCC} and the grid frequency ω_{PCC}, which are measured by a phase-locked loop (PLL) to ensure a smooth transition during the connection. Afterwards, an additional dynamic offset value $\Delta\hat{U}_{ctrl}$ can be added to the excitation to extend the VSM with a reactive power control or power system stabilizer (PSS). In [63,64], a resistive and reactive virtual impedance is included to represent the stator impedances of a machine. In the used implementation, these impedances are omitted since the transformer of the MMC acts as coupling impedance.

5. Scenarios Under Investigation

Two main network scenarios are considered for evaluation. The first scenario or scenario 1 (interconnected system) describes the complete, interconnected MVDC system with the interactions of the different assets and GFM control schemes. Here, the grids AC Grid 1 and 2 are operated with the MVDC link in full operation, allowing power to be transferred between the two AC grids to enable voltage and frequency support. In the second set of scenarios or scenario 2 (Islanded system), the focus is on the island operation of AC Grid 2, with a focus on the GFM capability of PRP and its services.

The complete interconnected test bench described in Figure 1 is considered. The steady-state operating points of the different assets under the various scenarios are summarized in Table 7. The power flow orientation is as indicated in Figure 1. Distinct events are emulated to assess the responses, the interactions, and the displaying of the various services of the different assets to stabilize the grid.

Table 7. MVDC/HVDC test bench steady-state operating points.

OP Scenario	(1a), (1b), (2a)	(1c1), (1c2)	(1d)	(2b1)
Linear Power Amplifier	**OFF**	**ON**	**OFF**	**OFF**
Grid 1				
$P_{AC,T1MV}$	+60	+60	+40	+60
$P_{AC,T2MV}$	+41	+41	+41	0
Const. Load *	−100	−100	−60	−100
Grid 2				
Conv PRP	+61	+67	+61	+61
Sim. PV	+20	+20	+20	+20
Const. Load *	−40	−40	−40	−40
LabMMC	0	0	0	0
Heating loads	0	−6	0	0

* Note: Negative power indicates load operation or consumption.

5.1. Scenario 1a—Inertia Provision with VSM Converter in Interconnected Topology

5.1.1. Scenario Description

This case describes the combined MVDC system response with a load step increase in Grid 1. Grid 1 and 2 are in steady-state operation. The progress of events are as follows: Both the interconnected Grid 1 and Grid 2 are under regular operation. A load step increase of 50 MW at load 1 of 50 MW is performed from its initial loading of 100 MW. The droop constants of DC-DC converters connected between HV/MV DC grids and MV/MV BESS are set to zero and hence do not participate in the DC voltage regulation with no power exchange with the HVDC grid. Grid 1, VSM control, and PRP scheme respond to stabilize the system. The responses of the GFM resources are monitored.

The PRP-interfaced GFM converter providing fast frequency response in coordination with the VSM control's inertial response is analyzed. The machine swing equation characterizes the inertial response of the VSM control modeled and adopted at medium-voltage Terminal 1 (T1MV). The energy control of T1MV obtains necessary energy via the DC network. MVAC Station T2 provides DC voltage support and draws power from MVAC

Grid 2 and hence the PRP-based converter. The power difference caused by the load step is eventually supplied by the generator grid equivalent in Grid 1.

5.1.2. Results and Inference

The plots displaying the response to the 50 MW load step are available in Figure 15. In this scenario, the droop-based primary frequency control of the VSM is deactivated. Thus, it does not contribute to the primary frequency control. It temporarily supports the fast frequency or so-called inertial response after the load step. After applying the load step, the VSM contributes with a fast frequency response to support and stabilize the frequency deviation together with the generator network equivalent. The frequencies of the generator network equivalent and the VSM change synchronously. The zoomed section of Figure 15 (VIII) qualitatively displays the response of the VSM, stabilizing the voltage in Grid 1 without any dips.

However, local-area oscillations are observed between the VSM-controlled converter and the upscaled generator network equivalent with low system inertia. The energy provided for the inertial support is retrieved from the MMC terminal T1MV and its internal energy, represented by $u_{\mathrm{SM},\Sigma 0,\mathrm{T1MV}}$, is balanced out via the DC side. The necessary balancing power is further retrieved from T2MV, which is balanced out via the AC side in Grid 2, as is visible in Figure 15 (V). Oscillations can be observed in the DC side powers and the internal energies of T1MV/T2MV after the load step. These result from the oscillatory control response of the total energy control and the DC current control of T1MV in the course of the sudden AC-side power retrieval. These oscillations are transmitted by T2MV to Grid 2 due to its DC voltage stabilization. Although the exchanged AC power of T1MV is measured and converted to a feed-forward reference of the DC current, the power measurement requires sufficient filtering, which results in a delay of the energy compensation leading to the oscillation. Although it is not analyzed in depth in this study, this observation shows that the delays of power and SM voltage filtering should be optimized with respect to power and SM voltage fluctuations. As the only GFM converter in Grid 2, the PRP-controlled converter provides the forwarded short-term energy. The PRP GFM control provides immediate fast frequency response to the event in coordination with the VSM control until Grid 1 or the generator equivalent takes over the primary control, as displayed in Figure 15. The stability of the interconnected networks is maintained, and the AC Grid 1 is supported with virtual inertia. Both VSM and PRP GFM control schemes return to their pre-disturbance operating points.

5.2. Scenario 1b—Load Increase in AC Grid 2 in Interconnected Topology

5.2.1. Scenario Description

The scenario displays the performance and interaction of the complete system with a focus on the control response of the PRP. The two networks, Grid 1 and Grid 2, with all connected loads and sources, are interconnected and in a steady state with constant PV infeed from Grid 2. A disturbance at Grid 2 is created by the connection and disconnection of the heating loads, creating a step event. The LabMMC is offline in this scenario. The event developments are described as follows. The LPA is initially offline. The three-phase heating loads are interfaced via the LPA, switched on, and consequently switched off after 3 s by disconnection of the LPA. The connection of the heating loads leads to the load step of approx. 6 MW. This scenario focuses on the GFM capability of the PRP-controlled converter in the course of sudden load steps. Hence, the converter's response and other resources are closely monitored.

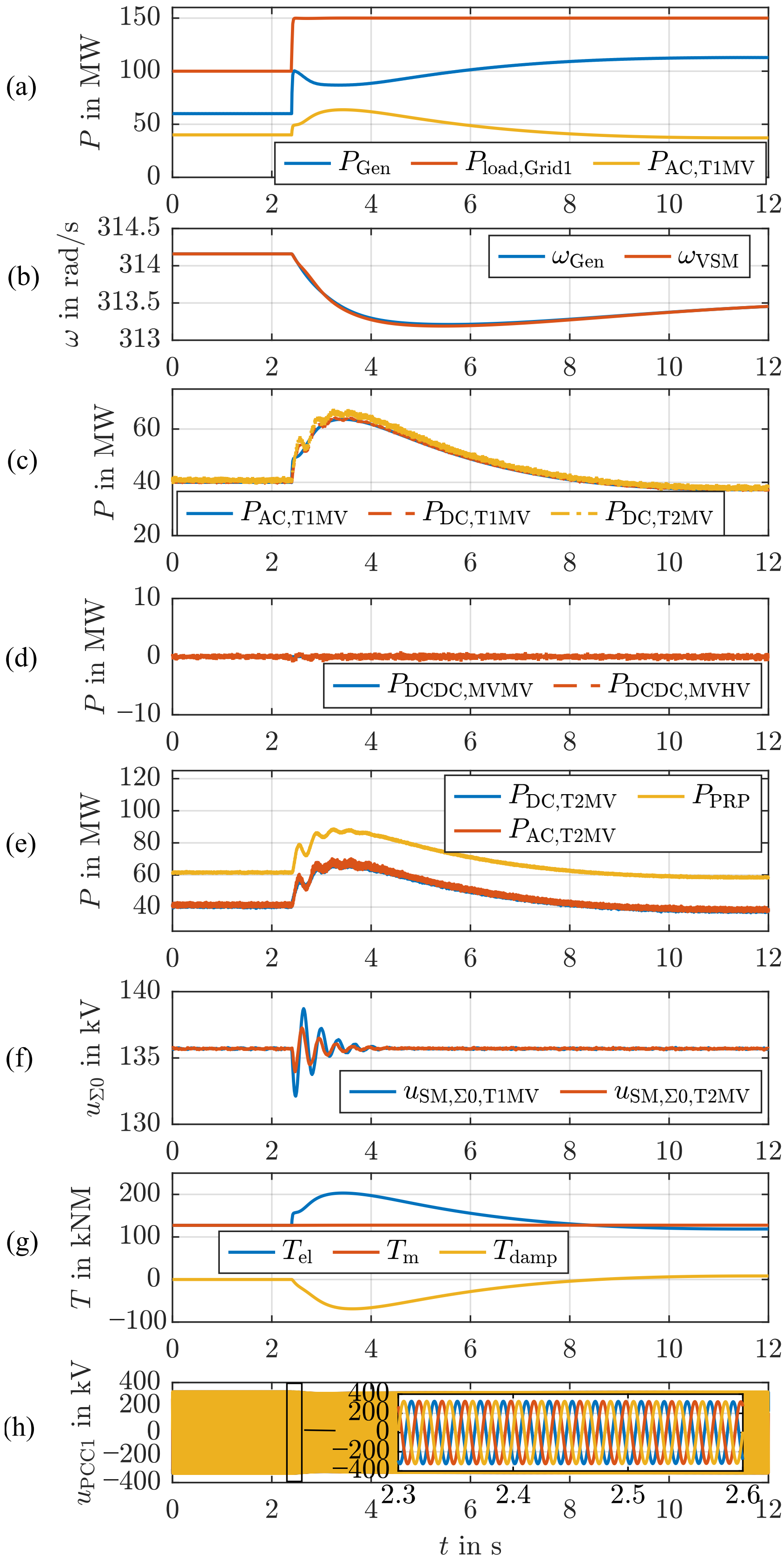

Figure 15. Scenario (1a) Inertia provision by VSM converter in interconnected topology. (**a**) AC powers of generator grid equivalent, load and T1MV in AC Grid 1. (**b**) Angular speed of generator grid equivalent and T1MV VSM. (**c**) AC and DC powers of T1MV and T2MV. (**d**) DC powers of DC-DC converters. (**e**) AC and DC powers of T2MV and PRP converter. (**f**) Average submodule sum voltage of MMC converter arms of T1MV and T2MV. (**g**) Virtual torques of T1MV VSM. (**h**) AC voltages at PCC1 in AC Grid 1.

5.2.2. Result and Inference

The plots displaying the responses are visible in Figure 16. The load resulting from the heating loads is stepped up by approx. 6 MW and stepped down by the same amount. The PRP immediately responds to the disturbance by stabilizing the grid voltage and frequency by taking over the entire load deviations of the power amplifier. The zoomed region in Figure 16 qualitatively demonstrates the response and shows the stabilizing effect without voltage dips. The measurement angle of the PRP is restored to its initial value before the event, thus generating a nominal frequency. The PRP-based GFM converter source supplies the power increase or decrease based on the load power variation, as represented by Figure 16. Grid 1 does not participate during the event, as shown in Figure 16e. Both controls of the LabMMC and the MVDC terminal T2MV remain in stable operation.

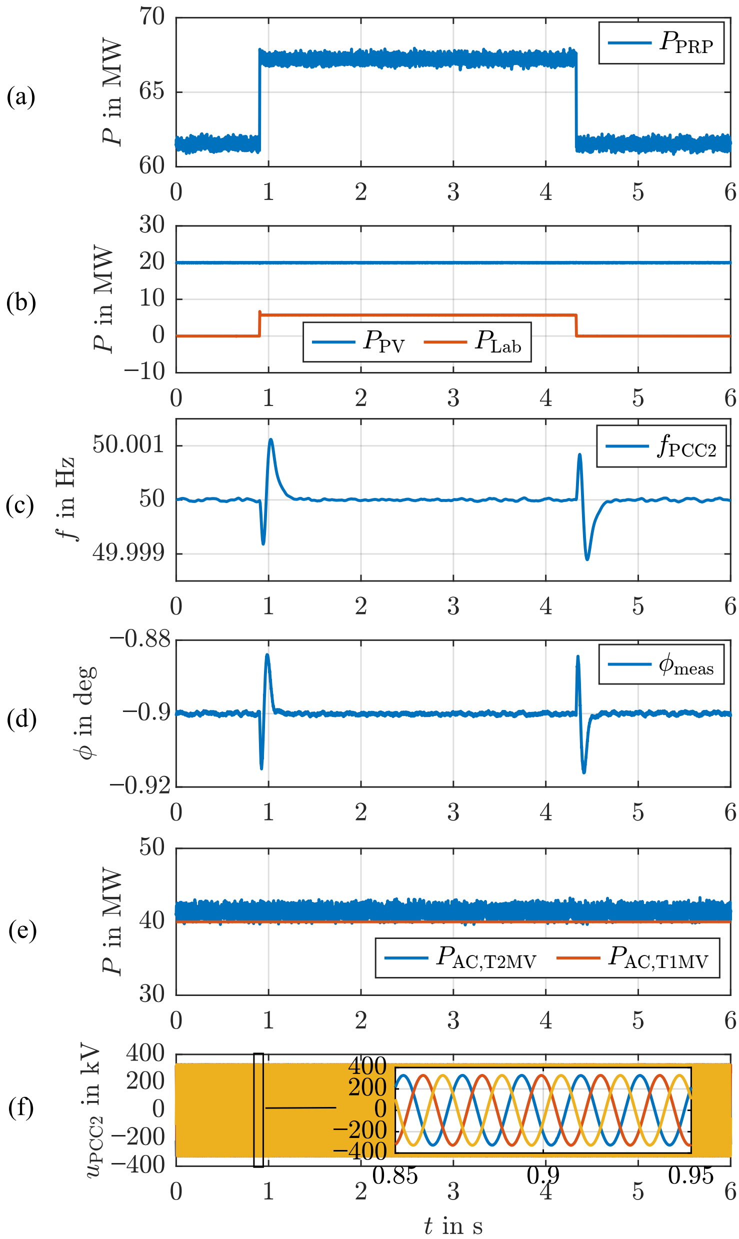

Figure 16. Scenario (1b) Load increase in AC Grid 2 in interconnected topology. (**a**) AC power of PRP converter. (**b**) AC powers of Microgrid-Lab and emulated PV. (**c**) Measured frequency AC Grid 2. (**d**) Voltage angle at node "meas" in AC Grid 2. (**e**) AC powers of T1MV and T2MV. (**f**) AC voltages at PCC2 in AC Grid 2.

5.3. Scenario 1c1—Power Forwarding for PRP Output Power Relief via DC-DC BESS

5.3.1. Scenario Description

This test case describes the response to a disturbance with additional setpoint adaptions applied to the interconnected system. The LabMMC is switched in multi-step load operation, with the entire system response evaluated for the step events. The actions include the following: The MMC is initially at 0 MW loading, with the heating loads at 6 MW consumption and the PV at 20 MW constant infeed. The droop constants of the HV/MV DC-DC converter and the MV/MV BESS DC-DC converter are zero with no participation, while the T2MV has a non-zero droop factor, thus being the only DC voltage-stabilizing converter in this scenario. Manual setpoint adaptations of the LabMMC via a Human–Machine Interface (HMI) are performed. The load step increase and decrease events are applied at the LabMMC in the following sequence: 0 MW→3 MW→6 MW→3 MW→0 MW. The T2MV and the BESS overtake power changes. T2MV reacts on behalf of the voltage power-droop control, while the DC-DC BESS converter acts on behalf of the power setpoint adaptations received from the power forwarding control. The active power loading is thus forwarded to the DC-DC BESS unit.

5.3.2. Result and Inference

This scenario describes the power-relieving avenues, while PRP delivers the fast frequency or inertial response. The power forwarding or overtake via the power setpoint adaptation of the DC-DC BESS converter after a load step on AC Grid 2 assists in the relief power infeed of PRP converter and increases the admissible power margin of the associated converter. In case of load steps in Grid 2 without further measures (case 2), the PRP-controlled converter provides fast frequency responses and permanently takes over the load changes of the connected LabMMC. In scenario 1c, the PRP delivers the response to the disturbance with temporary changes in the power output. However, the load steps are forwarded by measuring the increase in the PRP converter power output and the power-forwarding control to relieve the temporary power output of the PRP-based converter for further power imbalances. In scenario 1c1, the retrieved power of the LabMMC is stepped up and down, and both power setpoints of the terminal T2MV and the DCDC converter are dynamically adapted in order to relieve the PRP converter and provide the power changes via the BESS in the MVDC system. It can be seen that the original operating point of the PRP is restored within 2 s after each load change. All the responses are visible in Figure 17.

5.4. Scenario 1c2—Power Forwarding for PRP Output Power Relief via T1MV

5.4.1. Scenario Description

This test case is amended to case 1c1 by replacing the source of power dispatch from the DC-DC BESS unit to MVAC Grid 1 via T1MV. The rest of the procedure is identical. An immediate setpoint change is applied to the active power infeed at the node-marked PCC of Grid 2, which is forwarded as a setpoint change to T2MV and T1MV of the MVDC. The power setpoints of T2MV and T1MV are adapted synchronously by the power-forwarding control structure. The setpoint change of the LabMMC is performed via HMI while the setpoint adaptations of the other assets are derived from the measured power of the PRP-controlled converter and the power-forwarding control structure. The power dispatch is forwarded to MVAC Grid 1, relieving PRP's contribution to the event.

5.4.2. Result and Inference

This scenario describes the power-relieving approaches while PRP delivers the fast frequency or inertial response. The power forwarding or overtake via setpoint adaptation of the VSM-controlled T1MV after the load step on AC Grid 2 assists to relief power infeed of PRP converter and increases admissible power margin. In this case, the power is forwarded to AC Grid 1 instead of the BESS. The plots in Figure 18 describe the system responses. The power output of the PRP is restored after each load step. It can, however, be observed that the dynamics are slower compared to the power relief via the DC-DC BESS of scenario 1c1, as seen in Figure 18. The control structure of the VSM control explains this, since the power control of T1MV is handled as virtual mechanical torque. The power exchanged with AC Grid 1 is performed via its setpoint adaptation, which is dynamically delayed and slower than fast frequency responses. The DC droop control of T2MV counteracts its power setpoint adaptation until T1MV reaches its received new power setpoint. Based on the observations, it is concluded that the power forwarding to AC Grid 1 is functioning as expected with relatively fast power changes. However, it cannot be tracked as rapidly as with the DC control of the BESS DC-DC converter due to the high current and power control dynamics of the MV/MV DC-DC BESS converter. Please compare the plots in Figure 17 versus Figure 18 for a better overview.

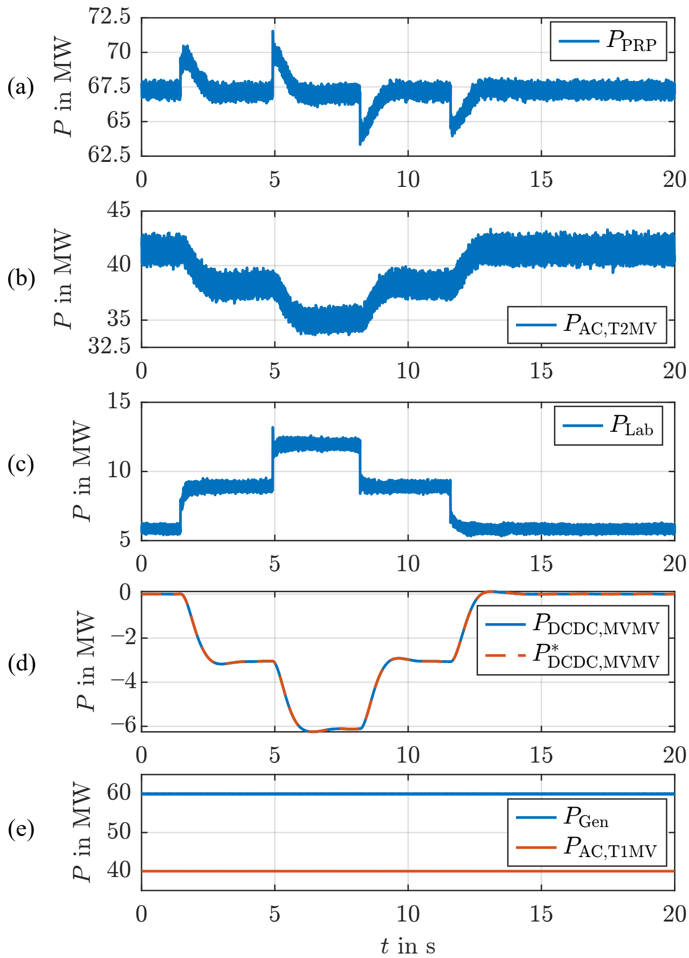

Figure 17. Scenario (1c1) Power forwarding for PRP output power relief via DC-DC BESS. (**a**) AC power of PRP converter. (**b**) AC power of T2MV. (**c**) AC power of Microgrid-Lab. (**d**) Measured and setpoint DC power of DC-DC BESS converter. (**e**) AC power of generator grid equivalent and T1MV in AC Grid 1.

5.5. *Scenario 1d—Islanding of AC Grid 1*

5.5.1. Scenario Description

To remain within the operational design limits of the VSM during the islanding, the load connected at PCC 1 is reduced from 100 to 60 MW compared to reference case 1a. The island scenario is created by isolating the generator representing the network equivalent from the remaining AC Grid 1 by disconnection via a breaker. Thus, creating an islanding operation of the MVDC with VSM in GFM mode and Grid 2 with PRP scheme in GFM control mode. The disconnection of the breaker performed is a dynamic event. The VSM GFM control provides inertial support. This event highlights the GFM capability of VSM control with the interconnected MVDC with Grid 2.

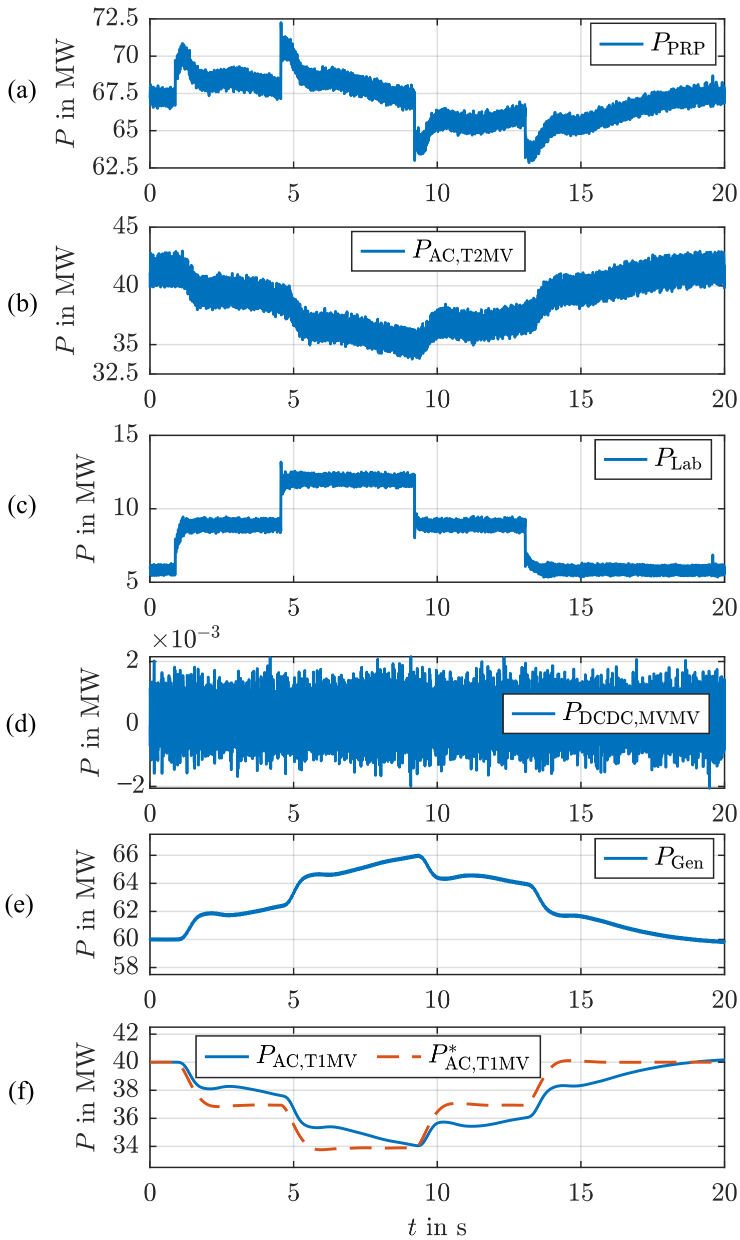

Figure 18. Scenario (1c2) Power forwarding for PRP output power relief via T1MV. (**a**) AC power of PRP converter. (**b**) AC power of T2MV. (**c**) AC power of Microgrid-Lab. (**d**) DC powers of DC-DC BESS converter. (**e**) AC power of generator grid equivalent in AC Grid 1. (**f**) Measured and setpoint AC power of T1MV.

5.5.2. Result and Inference

This case demonstrates the GFM capability of the VSM control under the critical event of islanding. The system responses are shown in Figure 19. In this case, the governor or primary frequency control of the VSM is activated to stabilize the grid frequency and voltage. The increased power infeed of the VSM ensures a further supply of the load after the loss of the rotating grid equivalent, balanced out via the DC grid and further by the PRP-controlled converter in AC Grid 2. The increase in power by the PRP and MVDC T2MV is visible in Figure 19b as a sudden energy variation introduced by the supply increase. These oscillations are transferred to the AC Grid 2 responses. Similar to scenario 1a, the sudden power change and the subsequent energy control action of T1MV causes non-negligible power oscillations on the DC side, which are transferred to AC Grid 2. This leads to the conclusion that the design of the total energy balancing control should be the subject of future analysis.

The following scenarios describe the island creation and stabilizing of AC Grid 2. With PRP as the only GFM source, its capabilities and services are demonstrated with the other assets in continued operation.

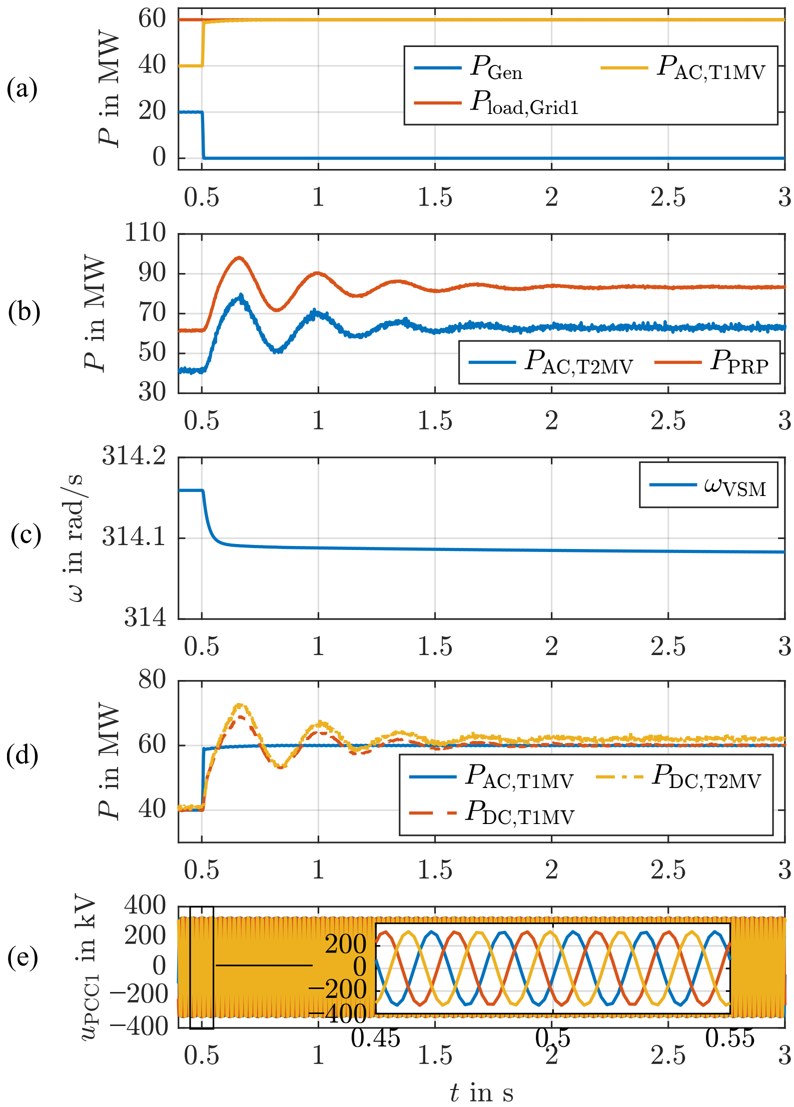

Figure 19. Scenario 1d) Islanding of AC Grid 1. (**a**) AC powers in AC Grid 1. (**b**) AC power of T2MV and Microgrid-Lab. (**c**) Angular speed of VSM T1MV. (**d**) AC and DC powers in MVDC grid. (**e**) AC voltages at PCC1 in AC Grid 1.

5.6. *Scenario 2a—Grid Separation of DC System and PRP AC Island*

5.6.1. Scenario Description

The island scenario is created by isolating the AC Grid 2 network by blocking station T2MV of the MVDC as a dynamic event at 0.5 s. Both DC-DC converters, MV/MV and MV/HV, take over the DC side power of MVDC terminal 1 (T1MV), which is still transmitted to Grid 1. The PRP GFM control scheme provides inertial support or fast frequency response and forms the AC network consisting of the Microgrid-Lab equipment and other simulated assets. The scenario description includes the initial steady-state normal operation of Grid 1 and Grid 2 with sufficient headroom in the PRP-controlled source. This scenario highlights the events in Grid 2 with PRP as the GFM asset. The GFM capability is demonstrated in case of sudden critical events, such as the blocking of a large converter as, e.g., terminal station T2MV, after an internal station fault.

5.6.2. Result and Inference

The successful islanding scenario of Grid 2 is witnessed. The AC power retrieved from T2MV drops rapidly at 0.5 s, leading to balancing reactions in the MVDC system and AC Grid 2. Based on its inherent disturbance-prioritizing characteristics over setpoint changes, PRP stabilizes the island, as visible in Figure 20c,d. It takes over the necessary power sharing as well. The PRP control restores the phase at its local measurement node measurement and grid frequency while maintaining a stable grid voltage with no visible voltage distortion.

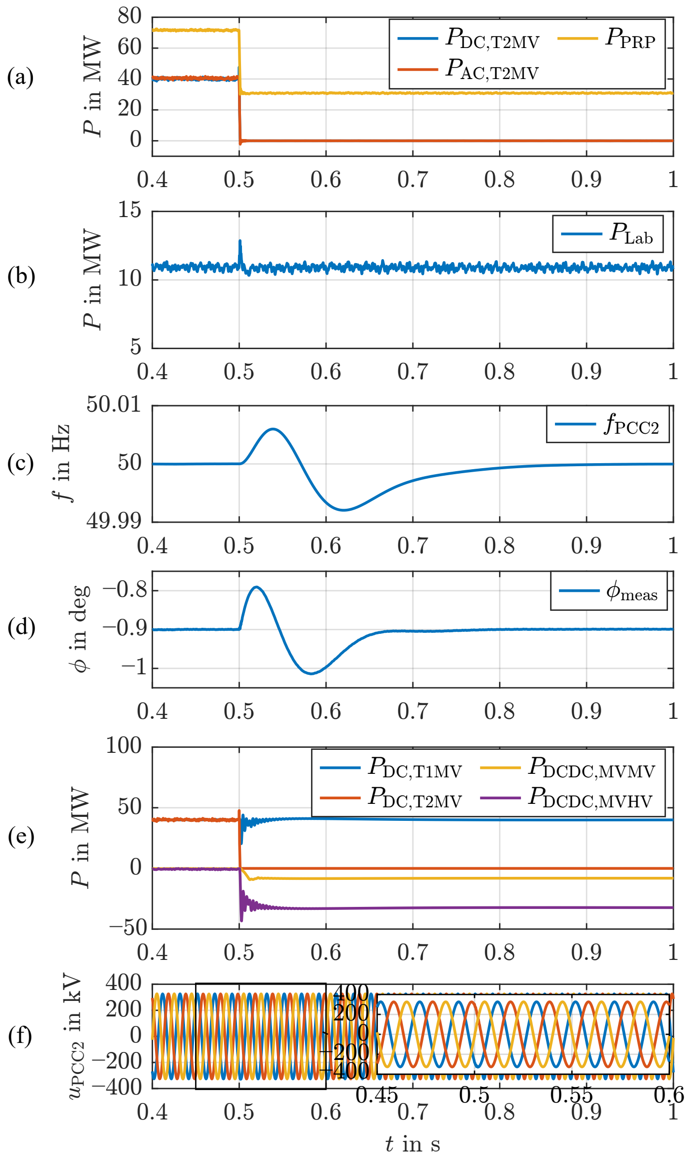

Figure 20. Scenario (2a) Grid separation of DC system and PRP AC island. (**a**) AC and DC powers at T2MV and PRP converter. (**b**) AC power of Microgrid-Lab. (**c**) Measured frequency AC Grid 2. (**d**) Voltage angle at node measured in AC Grid 2. (**e**) DC powers in MVDC grid. (**f**) AC voltages at PCC2 in AC Grid 2.

The Microgrid-Lab connected heating loads, the LabMMC, and the simulated PV thus remain stable despite the sudden event. All assets in Grid 2 remain connected with the same operating point, and the necessary plots are shown in Figure 20. On the DC side, the voltage droop controls of both DC-DC converters, the HV/MV converter and the MV/MV BESS converter, take over the sudden loss of T2MV by replacing the lost power supply.

5.7. Scenario 2b1—Grid Forming Capability of PRP in Islanded Topology with Steps in Static PV Infeed

5.7.1. Scenario Description

This test case is an addendum to Scenario 2a and displays additional disturbance in the island scenario by switching on and off the heating loads with constant PV injection. The successful creation and stabilization of the island Scenario 2a serves as the starting point for the events in this case. Grid 2 is in island operation with T2MV in blocking mode, and the heating loads are initially disconnected in the Microgrid-Lab. A steady-state operation of other sources and loads is maintained. The heating loads interfaced via LPA are switched on at approx. 1 s from the initially off position for approx. 3 s. It is then switched off at approx. 4 s. The connection and disconnection lead to load steps of approx. 6 MW. The MMC is offline in this scenario. PRP converter responds to the disturbance event, by a successive increase and decrease in its power infeed due to the variation of load step. Steady-state frequency is obtained. A stable operation of other elements on the island is witnessed.

5.7.2. Result and Inference

Scenario 2b1 focuses on PRP's response and services in the islanded system under disturbance. Providing an immediate response to the step event and restoring the phase, thus, nominal frequency in the network is displayed. The system is at a steady state prior to the event, and the initial power dispatches are seen in Figure 21. PRP provides a quick damped response to disturbances by restoring the phase in the system and stabilizing a prime differentiator of the control scheme, which is prominent with a small delay in scenario 2b1, with the on/off switching event of the heating loads as displayed in Figure 21d. After a small delay, the phase of the measurement voltage returns to its initial value after a short jump in the opposite direction, corresponding to steady state frequency. The converter equipped with the PRP control scheme has sufficient capacity and delivers adequate power to increased and decreased loading. The power response in Grid 2, as described by the active power trends in Figure 21a, is ripple-free due to blocked state of the MMC and the absence of the modulated voltage signals resulting from the switching-function MMC model during normal operation. Similar stable responses in island operation with PRP forming the network and adjusting its power infeed depending on the network requirements are displayed. The event responses are visible in Figure 21.

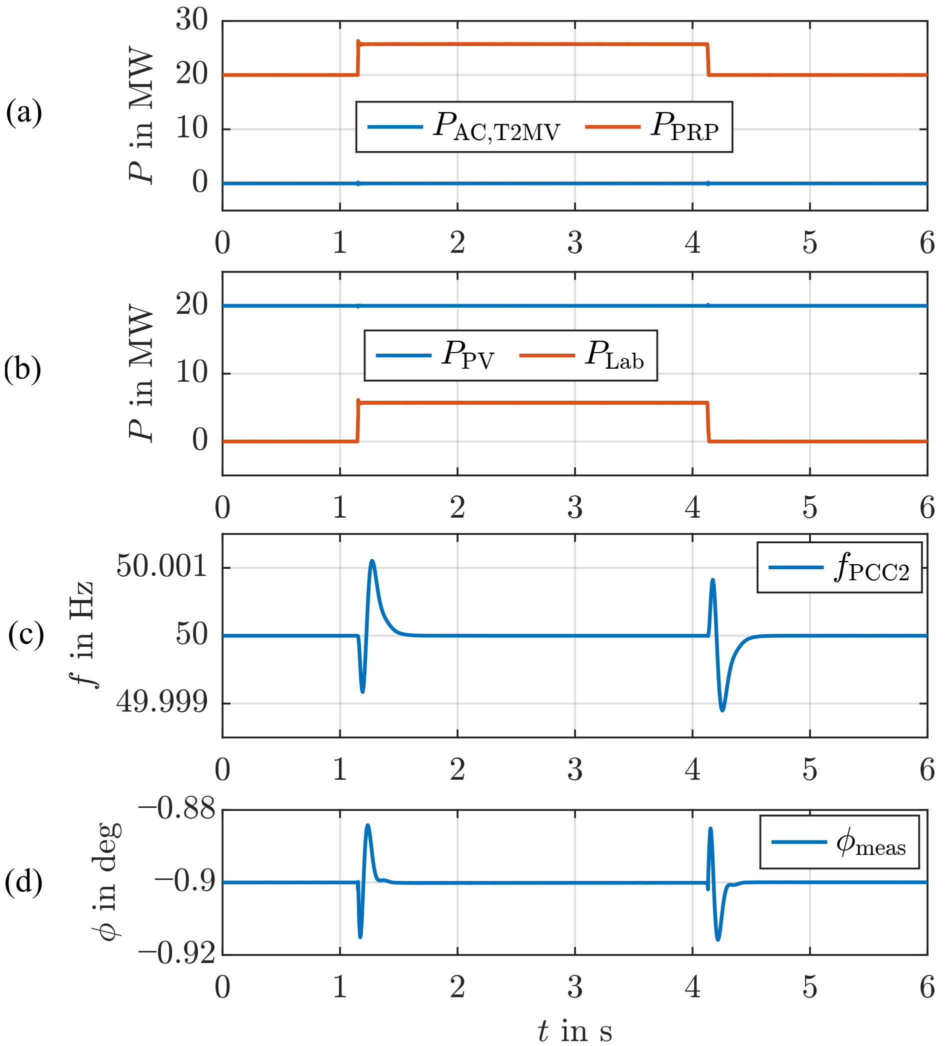

Figure 21. Scenario (2b1) Grid-forming capability of PRP in islanded topology with steps in static PV infeed. (**a**) AC powers at T2MV and PRP converter. (**b**) AC powers of Microgrid-Lab and emulated PV. (**c**) Measured frequency AC Grid 2. (**d**) Voltage angle at node measured in AC Grid 2.

6. Discussion and Outlook

6.1. Comparative Analysis with the State of Research

A comparative analysis with recent scientific publications in the field of control in hybrid AC/DC systems is presented below. This comparison focuses on studies examining GFM control in such systems, emphasizing its contribution to overall system stability. In contrast to research oriented towards secondary control, load flow management, or optimization, the selected publications highlight the role of GFM in ensuring the stable and reliable operation of hybrid AC/DC grids, underlining its potential to enhance system resilience.

The publications [28–30,35,65–68] represent significant contributions to GFM control in hybrid AC/DC networks. Their main focus is on optimizing control strategies, evaluating performance, and analyzing system services in hybrid AC/DC systems. Particular emphasis is placed on modular modeling approaches, innovative control techniques, and advanced converter technologies such as MMCs. These studies highlight that a key objective of current research is to enhance system stability through frequency and voltage support, thereby increasing the robustness of hybrid AC/DC grids, particularly under dynamic and fault conditions.

Given the scope of this work, the following analysis concentrates on publications using HiL setups to ensure comparability. Table 8 provides a summary comparing various publications in the field of GFM control in hybrid AC/DC systems using HiL setups. The comparison distinguishes between the studied systems and the focus of the simulation scenarios. The system descriptions categorize whether heterogeneous systems with GFL, GFM, and SynM are studied, whether multi-terminal DC systems are analyzed, and whether the AC grid models are based on extensive real-life networks. The simulation scenarios indicate the emphasis on PHiL setups and system stability, as well as whether interoperability and islanding are examined. This work is particularly distinct from other publications listed in the table due to its extensive multi-terminal, voltage-level-spanning MVDC/HVDC system and its focus on interoperability of various control strategies and subsystems within the overall system. The simulation results demonstrate the interoperability of numerous actors instead of concentrating on a specific control optimization, which is the primary focus of many publications in this area. A comparison of scenarios and results between this work and these publications highlights the promising performance of PRP control, even under extreme scenarios. It provides a rapidly damped response to disturbances and demonstrates interoperability with other control strategies, suggesting that further investigation into PRP is worthwhile.

Table 8. Focus areas of HiL investigations in various publications on GFM control in hybrid systems.

	System Under Study			Simulation Scenarios			
	Heterogeneous System	**DC Multi-Terminal**	**Large AC System**	**PHiL**	**System Stability**	**Interoperability**	**Islanding**
This paper	xx	xx	-	x	xx	xx	xx
[28]	-	-	-	x	x	x	x
[29]	x	-	-	xx	xx	x	-
[30]	xx	-	xx	xx	xx	-	x
[35]	xx	-	xx	-	x	x	-
[66]	-	-	-	x	x	-	xx

-: Not considered; x: Part of the investigations; xx: Main focus of the investigations

In addition, publications [65,66] underscore the importance of further exploration in the area of small-signal stability in hybrid systems. While a small-signal stability analysis for PRP control has been published in [10], such investigations are not conducted for the hybrid AC/DC test system presented here. Against this backdrop, the publications [65,66] are discussed in greater detail below. A hybrid system comprising HVDC and renewable AC sources is investigated in publication [65]. While the general setup is comparable to the present work, significant methodological differences exist, particularly the use of small-signal stability analysis. This difference prevents a direct comparison at this stage but underscores the relevance of the study, as small-signal stability is a critical aspect of system stability and is planned for investigation in future work. Publication [66] implements a dual-port GFM controller in a hybrid system with MMC converters, examining it through both small-signal stability and HiL setups. The HiL configuration is significantly less comprehensive compared to this work. Nevertheless, it highlights the relevance of combining analytical and experimental approaches to evaluate dynamic stability in hybrid AC/DC systems. The dual-port GFM control approach, where one controller simultaneously forms both AC and DC systems, represents an interesting application for the developed test system in this paper.

6.2. Limitations of the Investigations and Outlook

This study focuses on investigating the interaction of different control strategies in a heterogeneous grid, rather than comparing the performance of these strategies. The test system is developed to validate a novel GFM control approach, the Phase-Restoring Principle, using HiL methods. One objective is to demonstrate that the PRP-based control can operate in parallel with a real GFL inverter, integrated into the setup via PHiL. Even under extreme scenarios, such as an abrupt transition to islanded operation where the PRP has to stabilize the entire grid, the laboratory inverter remains operational without any disturbances. Of note, the laboratory inverter is designed for low-voltage applications and scaled up to emulate higher voltage levels, a common practice in PHiL experiments [69–71]. While this scaling can reduce the plausibility of results for a PHiL setup, it is not a limiting factor in this context because the LabMMC is not the device under test but the PRP control. In fact, the results are conservative because, according to standards such as [72], low-voltage converters typically have less stringent power-quality requirements ($THD \leq 8\%$) compared to high-voltage inverters ($THD \leq 2.5\%$). For instance, high-voltage MMCs are distinguished by a significantly greater number of levels, enabling them to deliver superior power quality.

A variety of scenarios has been analyzed, including those with increased participation of the HVDC system. However, only a selected subset of these scenarios is presented in this paper. In all cases, a positive impact on system stability is observed. Nevertheless, no scenarios have been conducted on PRP in parallel operation with the LabMMC in GFM mode. Similarly, no tests have been performed on parallel grid operation with a PHiL SynM. This has been investigated analytically and offline, but practical proof is still lacking. In the meantime, the laboratory has been upgraded with a 45.2 kVA SynM, enabling such validations in the future.

Also, no current-limiting functionality in both the VSM and PRP control is implemented. This was an intentional choice to focus solely on analyzing the control behavior. Research on current limiting for GFM controls is available in the literature [73–76], and a specific current-limiting strategy for the PRP has been developed but not yet published.

In addition, the battery management system of the BESS is not modeled in the MVDC circuit. Also, grid-protection mechanisms are not modeled and the test system is integrated into simplified AC equivalents rather than larger networks. While these simplifications are sufficient for the intended investigations, future research should focus on integrating GFM controls into bulk power systems, evaluating system stability, and gaining operational experience, particularly in conjunction with grid-protection systems.

As the next step, a GFM hybrid plant will be modeled in the test system, following a similar concept as in [29]. The hybrid plant consists of a GFM battery with PRP control and a dynamic PV infeed. A power-plant controller implemented on a SICAM A8000 will coordinate the operation of the hybrid plant in a CHiL test setup. GFM hybrid power plants remain a largely unexplored area in scientific research. While [29,77] provide some insights on this topic, the practical application of PRP to a real inverter and its testing under laboratory or field conditions remains pending.

Furthermore, the test system offers potential for future research in system theory and stability analysis, including small-signal stability in DC grids. Studies [65,66] can serve as a reference for this purpose.

In the long term, GFM controls such as PRP or VSM should be integrated into larger real-life power system models (e.g., bulk power systems), assessed for their impact on system stability, and tested alongside grid-protection schemes. The Kopernikus ENSURE Co-Demonstration Platform [33] provides a suitable tool for these advanced investigations.

7. Conclusions

The transition to a converter-dominated power system, driven by the continuous increase in inverter-based resources, introduces novel stability challenges to the grid. The deployment of various GFM and GFL control strategies may lead to undesirable interactions, potentially resulting in critical situations in weak-grid or islanding scenarios.

Moreover, emerging grid structures, such as MVDC networks, are expected to transform future power systems into hybrid, interconnected systems.

In order to identify and address these challenges at an early stage, the extensive testing of advanced control strategies under high-fidelity conditions is mandatory. This research introduces a hybrid demonstrator designed for the modular evaluation of novel GFM control strategies within hybrid AC/DC configurations across multiple voltage levels. The demonstrator is implemented in a real-time EMT simulation environment, providing a flexible PHiL interface for integrating real hardware.

In this work, two GFM control strategies are evaluated: the state-of-the-art VSM control and the recently developed PRP control. These strategies are tested in the demonstrator under weak-grid and islanding conditions, with the PRP response further validated in a PHiL setup. The PRP control demonstrates its ability to respond to disturbances by adjusting the setpoints, achieving nominal frequency with minimal phase shift at the measurement node (ϕ_{meas}) and transitioning to a new operating point via a direct control path. The VSM control is deployed at the MVDC terminal, leveraging its stabilizing properties. This AC-side converter control emulates SynM dynamics, providing short-term inertia to mitigate frequency deviations and optional long-term proportional frequency support while maintaining synchronization with the rotating AC grid. However, careful consideration must be given to the energy balancing of the VSM MMC to prevent local-area oscillations with SynM in scenarios with low inertia. Furthermore, the demonstrator incorporates innovative power setpoint adaptation mechanisms, such as the adjustment of droop characteristics on the DC side. This enables flexible power dispatch, allowing for control over the contributions from individual sources and adaptation to varying scenarios, thereby enhancing operational flexibility in response to subsequent disturbances.

Future work will involve the implementation of a CHiL interface to facilitate the integration of real plant and converter controllers, thereby further enhancing the realism and adaptability of the demonstrator.

Author Contributions: Conceptualization, M.R., A.K. and G.M.; methodology, M.R., A.K., J.R., T.W. and S.H.; software, M.R., A.K., J.R., T.W. and S.H.; validation, M.R. and A.K.; formal analysis, M.R. and A.K.; investigation, M.R., A.K., J.R. and T.W.; resources, G.M.; data curation, J.R.; writing—original draft preparation, M.R., A.K. and J.R.; writing—review and editing, M.R., A.K., J.R., T.W. and G.M.; visualization, M.R., A.K. and J.R.; supervision, G.M.; project administration, G.M.; funding acquisition, G.M. All authors have read and agreed to the published version of the manuscript.

Funding: This research was funded by the German Federal Ministry of Education and Research (BMBF) within the Kopernikus Project ENSURE 'New ENergy grid StructURes for the German Energiewende'.

Data Availability Statement: The original contributions presented in this study are included in the article. Further inquiries can be directed to the corresponding author.

Acknowledgments: The authors gratefully acknowledge funding by the German Federal Ministry of Education and Research (BMBF) within the Kopernikus Project ENSURE 'New ENergy grid StructURes for the German Energiewende'. They would also like to thank Stephan Rupp and Sebastian Brüske from Maschinenfabrik Reinhausen GmbH, Germany for their support.

Conflicts of Interest: Author Ananya Kuri was employed by the company Siemens AG Foundational Technologies. Author Stefan Henninger was employed by the company Fluence Energy GmbH. The remaining authors declare that the research was conducted in the absence of any commercial or financial relationships that could be construed as a potential conflict of interest.

Nomenclature

Abbreviations

3p-DAB	Three-Phase Dual Active Bridge
BESS	Battery Energy-Storage System
CHiL	Control-Hardware-in-the-Loop
DAB	Dual Active Bridge
GFL	Grid-Following
GFM	Grid-Forming
HiL	Hardware-in-the-Loop
HMI	Human–Machine Interface
HV	High Voltage
HVDC	HighVoltage Direct Current
ISOP	Input-Series-Output-Parallel
LPA	Linear Power Amplifier
LV	Low Voltage
MMC	Modular Multilevel Converter
MT	Multi-Terminal
MV	Medium Voltage
MVDC	Medium-Voltage Direct Current
PHiL	Power-Hardware-in-the-Loop
PRP	Phase-Restoring Principle
PV	Photovoltaic
SIPO	Serial Input, Parallel Output
SM	Submodule
SynM	Synchronous Machine
TYNDP	Ten Years Network Development Plan
VISMA	Virtual Synchronous Machine

Common for all MMC based controls

i_{g}^{*}	Reference of grid currents
θ_{PCC}	Grid angle at PCC from PLL
$u_{\mathrm{abc,PCC}}$	Grid voltages measured at PCC
$u_{\mathrm{g,abc}}^{*}$	MMC control voltage component from grid current control
$u_{\mathrm{c,abc}}^{*}$	MMC control voltage component from inner circulating-current control
$u_{\mathrm{U/L,abc}}^{*}$	MMC arm reference voltages
$m_{\mathrm{U/L,abc}}^{*}$	MMC arm reference modulation indexes
u_{SM}	Individual measured internal submodule voltages
$u_{\Sigma\mathrm{SM,arm}}$	Sum of internal submodule voltages for each MMC arm
i_{arm}	Measured currents of MMC arms
$i_{\mathrm{g},W_{\mathrm{tot}}}^{*}$	Ref. of grid current from total energy-balancing control
i_{c}^{*}	Ref. of inner circulating currents derived from balancing control

MMC based DC-DC control

$i_{\mathrm{c},W_{\Sigma\Delta,\alpha\beta}}^{*}$	Ref. of inner circulating currents from balancing control
$I_{\mathrm{DC},P_{\mathrm{DC}}}^{*}$	Ref. of DC current from voltage droop control
$i_{\mathrm{d},W_{\mathrm{tot}}}^{*}$	Ref. of AC current direct component from total energy balancing via AC-side
$u_{\Sigma,\mathrm{abc}}^{*}$	MMC control voltage component from AC side current control
$u_{\Delta,\mathrm{abc}}^{*}$	MMC control voltage component from inner circulating-current control
$i_{\mathrm{d},P_{\mathrm{DC}}}^{*}$	Ref. of AC current direct component from voltage droop control
$i_{\mathrm{DC-HV,ff},P_{\mathrm{DC}}}^{*}$	Ref. feed-forward DC current for HV MMC from voltage droop control
θ	Ref. AC grid voltage angle for HV MMC

MMC grid-forming VSM control	
$P_{\mathrm{el,PCC}}$	Active power measured at PCC
$\hat{U}_{\mathrm{PCC}}$	Voltage magnitude measured at PCC from PLL
$i_{\mathrm{DC,ff}}$	VSM Feed-forward reference value of DC current for energy balancing
$u^{*}_{\mathrm{g,abc,VSM}}$	MMC control voltage component from grid current control
P_{m}	Virtual mechanical power of VSM used as power setpoint
T_{m}	Virtual mechanical torque of VSM
T_{e}	Virtual electrical torque of VSM
T_{Damp}	Damping torque of VSM
K_{d}	Damping constant
K_{gov}	Primary droop constant for primary frequency support
w_{n}	Nominal angular speed
w_{VSM}	Virtual angular speed of VSM
θ_{VSM}	Virtual rotor angle of VSM
MV/MV DC-DC 3p-DAB control	
P^{*}_{DC}	Reference total DC power
$P^{*}_{\mathrm{DC,SM}}$	Reference DC power per SM
$i^{*}_{\mathrm{s,SM}}$	Reference value of secondary DC current of DAB SM
ϕ_{ff}	Feed-forward term of phase shift angle
f_{s}	Switching frequency
L_{σ}	Stray impedance of coupling transformer
a_{T}	Voltage ratio of coupling transformer
$n_{\mathrm{SM,3p-DAB}}$	Number of parallel submodules
$u_{\mathrm{n,p}}$	Nominal primary DC voltage
$u_{\mathrm{s,filt}}$	Filtered secondary DC voltage
N/D	Division Block (Numerator/Denominator)
PRP control	
$u_{\mathrm{m,123}}$	Measurement voltage input
$u_{\mathrm{c,123}}$	Converter voltage output
P_{m}	Measured active power
P_{ref}	Reference value of active power
S_{n}	Rating of the converter
F_{n}	Nominal frequency
F_{dr}	Drift frequency
ϑ_{dr}	Phase drift due to an event
$\vartheta_{\mathrm{n}} - \vartheta_{\mathrm{dr}}$	Transformation angle over the feedback loop in PRP control
$\vartheta_{\mathrm{n}} + \vartheta_{\mathrm{dr}}$	Transformation angle in ideal PLL control
U_{n}	Reference voltage at measurement node
φ_{0}	Initial phase at the measurement node
T	Measurement delay
$S\&H$	Sample and hold
T_{A}	Sampling time constant
T_{1}	Time constant
T_{2}	Time smoothing constant
T_{2}	Active power controller (APC) time constant
K_{1}	Voltage magnitude gain
K_{2}	Self-stabilizing APC power-frequency droop
K_{2}	APC gain
$\rho_{\mathrm{dr}}\iota_{\mathrm{dr}}$	New coordinate system in PRP control due to the frequency drift

References

1. Hatziargyriou, N.; Milanović, J.; Rahmann, C.; Ajjarapu, V.; Cañizares, C.; Erlich, I.; Hill, D.; Hiskens, I.; Kamwa, I.; Pal, B.; et al. *Stability Definitions and Characterization of Dynamic Behavior in Systems with High Penetration of Power Electronic Interfaced Technologies*; IEEE PES Technical Report PES-TR77; IEEE: Piscataway, NJ, USA, 2020.
2. Meegahapola, L.; Sguarezi, A.; Bryant, J.S.; Gu, M.; Conde D, E.R.; Cunha, R.B. Power system stability with power-electronic converter interfaced renewable power generation: Present issues and future trends. *Energies* **2020**, *13*, 3441. [CrossRef]
3. Kocewiak, L.; Blasco-Giménez, R.; Buchhagen, C.; Kwon, J.B.; Sun, Y.; Trevisan, A.S.; Larsson, M.; Wang, X. Overview, status and outline of stability analysis in converter-based power systems. In Proceedings of the 19th International Workshop on Large-Scale Integration of Wind Power into Power Systems as Well as on Transmission Networks for Offshore Wind Plants, Virtual, 11–12 November 2020; pp. 11–12.
4. Wachter, J.; Gröll, L.; Hagenmeyer, V. Survey of Real-World Grid Incidents–Opportunities, Arising Challenges and Lessons Learned for the Future Converter Dominated Power System. *IEEE Open J. Power Electron.* **2024**, *5*, 50–69. [CrossRef]
5. Muenz, U.; Xue, N.; Wu, X.; Mesanovic, A.; Cockcroft, L.; Dangelmaier, L.; Heyde, C.; Dong, Z.; Chakraborty, S.; Ashok, A. Operational Security in 100% Inverter-Based Power Systems: Experiences from Hawaii. *IEEE Electrif. Mag.* **2022**, *10*, 10–19. [CrossRef]
6. Musca, R.; Vasile, A.; Zizzo, G. Grid-forming converters. A critical review of pilot projects and demonstrators. *Renew. Sustain. Energy Rev.* **2022**, *165*, 112551. [CrossRef]
7. Rathnayake, D.B.; Akrami, M.; Phurailatpam, C.; Me, S.P.; Hadavi, S.; Jayasinghe, G.; Zabihi, S.; Bahrani, B. Grid Forming Inverter Modeling, Control, and Applications. *IEEE Access* **2021**, *9*, 114781–114807. [CrossRef]
8. Lin, Y.; Eto, J.H.; Johnson, B.B.; Flicker, J.D.; Lasseter, R.H.; Villegas Pico, H.N.; Seo, G.S.; Pierre, B.J.; Ellis, A. *Research Roadmap on Grid-Forming Inverters*; NREL/TP-5D00-73476; National Renewable Energy Laboratory (NREL): Golden, CO, USA, 2020. Available online: https://www.nrel.gov/docs/fy21osti/73476.pdf (accessed on 12 December 2024).
9. Rosso, R.; Wang, X.; Liserre, M.; Lu, X.; Engelken, S. Grid-Forming Converters: Control Approaches, Grid-Synchronization, and Future Trends—A Review. *IEEE Open J. Ind. Appl.* **2021**, *2*, 93–109. [CrossRef]
10. Kuri, A.; Zurowski, R.; Mehlmann, G.; Audring, D.; Luther, M. A Novel Grid Forming Control Scheme Revealing a True Inertia Principle. *IEEE Trans. Power Syst.* **2021**, *36*, 5369–5384. [CrossRef]
11. Kuri, A.; Zurowski, R.; Mehlmann, G.; Luther, M. Power Dispatch Capacity of a Grid-Forming Control Based on Phase Restoring Principle. *IEEE Syst. J.* **2022**, *17*, 3389–3400. [CrossRef]
12. Kuri, A.; Raab, A.; Takhtaganov, A.; Mehlmann, G.; Luther, M.; Kuri, A. Comparison of Phase Restoring Principle with other Grid-Forming Methodologies. In Proceedings of the 2023 IEEE Power and Energy Society General Meeting (PESGM), Orlando, FL, USA, 16–20 July 2023; pp. 1–5. [CrossRef]
13. Rupp, S.; Graeme, B.; Schichler, U. MVDC Grids to Facilitate the Roll Out of Renewables. In Proceedings of the 2023 27th International Conference on Electricity Distribution, Rome, Italy, 12–15 June 2023.
14. De Carne, G.; Maroufi, S.M.; Beiranvand, H.; De Angelis, V.; D'Arco, S.; Gevorgian, V.; Waczowicz, S.; Mather, B.; Liserre, M.; Hagenmeyer, V. The role of energy storage systems for a secure energy supply: A comprehensive review of system needs and technology solutions. *Electr. Power Syst. Res.* **2024**, *236*, 110963. [CrossRef]
15. CIGRE. *Medium Voltage DC Distribution Systems: Reference: 875*; CIGRE WG C6/B4.37; CIGRE: Paris, France, 2022. Available online: https://www.e-cigre.org/publications/detail/875-medium-voltage-dc-distribution-systems.html (accessed on 12 December 2024).
16. CIGRE. *Medium Voltage Direct Current (MVDC) Grid Feasibility Study: Technical Brochure 793*; CIGRE WG C6.31; CIGRE: Paris, France, 2020. Available online: https://www.e-cigre.org/publications/detail/793-medium-voltage-direct-current-mvdc-grid-feasibility-study.html (accessed on 12 December 2024).
17. Larruskain, D.M.; Zamora, I.; Abarrategui, O.; Aginako, Z. Conversion of AC distribution lines into DC lines to upgrade transmission capacity. *Electr. Power Syst. Res.* **2011**, *81*, 1341–1348. [CrossRef]
18. Westermann, D.; Schlegel, S.; Sass, F.; Schwerdfeger, R.; Wasserrab, A.; Haeger, U.; Dalhues, S.; Biele, C.; Kubis, A.; Hachenberger, J. Curative actions in the power system operation to 2030. In Proceedings of the International ETG-Congress 2019, Esslingen am Neckar, Germany, 8–9 May 2019; pp. 1–6.
19. Coffey, S.; Timmers, V.; Li, R.; Wu, G.; Egea-Àlvarez, A. Review of MVDC Applications, Technologies, and Future Prospects. *Energies* **2021**, *14*, 8294. [CrossRef]
20. Qin, H.; Wu, R.; Abd-el Motaleb, A.M.; Ran, L.; Deng, X.; Sensarma, P. Utilisation of back-to-back VSC in a distribution network with DG. In Proceedings of the 2016 IEEE International Conference on the Science of Electrical Engineering (ICSEE), Eilat, Israel, 16–18 November 2016; pp. 1–5. [CrossRef]
21. Zhang, L.; Liang, J.; Tang, W.; Li, G.; Cai, Y.; Sheng, W. Converting AC Distribution Lines to DC to Increase Transfer Capacities and DG Penetration. *IEEE Trans. Smart Grid* **2019**, *10*, 1477–1487. [CrossRef]

22. Yu, J.; Smith, K.; Urizarbarrena, M.; MacLeod, N.; Bryans, R.; Moon, A. Initial designs for the Angle DC project; converting existing AC cable and overhead line into DC operation. In Proceedings of the 13th IET International Conference on AC and DC Power Transmission (ACDC 2017), Manchester, UK, 14–16 February 2017. [CrossRef]
23. Sun, K.; Li, K.J.; Wang, M.; Tian, G.; Wang, Z.d.; Liu, Z. Coordination control for multi-voltage-level dc grid based on the dc–dc converters. *Electr. Power Syst. Res.* **2020**, *178*, 106050. [CrossRef]
24. Salcedo, R.; Nowocin, J.; Smith, C.; Rekha, R.; Corbett, E.; Limpaecher, E.; LaPenta, J. *Development of a Real-Time Hardware-in-the-Loop Power Systems Simulation Platform to Evaluate Commercial Microgrid Controllers*; Technical Report TR-1203; Lincoln Laboratory, MIT: Boston, MA, USA, 2016.
25. Lauss, G.F.; Faruque, M.O.; Schoder, K.; Dufour, C.; Viehweider, A.; Langston, J. Characteristics and design of power hardware-in-the-loop simulations for electrical power systems. *IEEE Trans. Ind. Electron.* **2015**, *63*, 406–417. [CrossRef]
26. Edrington, C.S.; Steurer, M.; Langston, J.; El-Mezyani, T.; Schoder, K. Role of power hardware in the loop in modeling and simulation for experimentation in power and energy systems. *Proc. IEEE* **2015**, *103*, 2401–2409. [CrossRef]
27. Kikusato, H.; Orihara, D.; Hashimoto, J.; Takamatsu, T.; Oozeki, T.; Matsuura, T.; Miyazaki, S.; Hamada, H.; Miyazaki, T. Performance evaluation of grid-following and grid-forming inverters on frequency stability in low-inertia power systems by power hardware-in-the-loop testing. *Energy Rep.* **2023**, *9*, 381–392. [CrossRef]
28. Babu, V.V.; Roselyn, J.P.; Nithya, C.; Sundaravadivel, P. Development of Grid-Forming and Grid-Following Inverter Control in Microgrid Network Ensuring Grid Stability and Frequency Response. *Electronics* **2024**, *13*, 1958. [CrossRef]
29. Gevorgian, V.; Wallen, R.; Koralewicz, P.; Mendiola, E.; Shah, S.; Morjaria, M. *Provision of Grid Services by PV Plants with Integrated Battery Energy Storage System: Preprint*; NREL/CP-5D00-78140; National Renewable Energy Laboratory (NREL): Golden, CO, USA, 2020. Available online: https://research-hub.nrel.gov/en/publications/provision-of-grid-services-by-pv-plants-with-integrated-battery-e (accessed on 12 December 2024).
30. Hoke, A.; Koralewicz, P.; Kenyon, R.W.; Wang, B.; Yu, L.; Kawamura, K.; Tan, J. Stabilizing Inverter-Based Transmission Systems: Power hardware-in-the-loop experiments with a megawatt-scale grid-forming inverter. *IEEE Electrif. Mag.* **2022**, *10*, 32–44. [CrossRef]
31. Federal Ministry for Economic Affairs and Climate Action (BMWK). *System Stability Roadmap—Roadmap for Achieving the Secure and Robust Operation of the Future Power Supply System with 100% Renewable Energy Sources;* BMWK: Berlin, Germany, 2023.
32. Benigni, A.; Strasser, T.; De Carne, G.; Liserre, M.; Cupelli, M.; Monti, A. Real-Time Simulation-Based Testing of Modern Energy Systems: A Review and Discussion. *IEEE Ind. Electron. Mag.* **2020**, *14*, 28–39. [CrossRef]
33. Mehlmann, G.; Kühnapfel, U.; Wege, F.; Winkens, A.; Scheibe, C.; Vogel, S.; Noglik, P.; Gratza, M.; Richter, J.; Weber, M.; et al. The Kopernikus ENSURE Co-Demonstration Platform. *IEEE Open J. Power Electron.* **2023**, *4*, 987–1002. [CrossRef]
34. Vogel, S.; Mirz, M.; Razik, L.; Monti, A. An open solution for next-generation real-time power system simulation. In Proceedings of the 2017 IEEE Conference on Energy Internet and Energy System Integration (EI2), Beijing, China, 26–28 November 2017. [CrossRef]
35. Richter, J.; Burlakin, I.; Wagner, T.; Richter, M.; Mehlmann, G.; Luther, M. Integration of a Grid-Forming MVDC-System into a Transmission Grid Section for Real-Time Applications. In Proceedings of the 8th IEEE Workshop on the Electronic Grid, Karlsruhe, Germany, 16–18 October 2023; pp. 1–6. [CrossRef]
36. Dennetière, S.; Nguefeu, S.; Saad, H.; Mahseredjian, J. Modeling of modular multilevel converters for the France-Spain link. *Star* **2013**, *2*, 4.
37. Buchner, A.; Schichler, U. Application of extruded MVAC Cables for DC Power Transmission. In Proceedings of the 10th International Conference on Insulated Cables, Paris, France, 23–27 June 2019.
38. Surawijaya, S.; Buchner, A.A.; Schichler, U.; Suwarno. Investigation of the Possibility to Convert Medium Voltage AC Overhead Lines (OHL) to DC. In Proceedings of the 2020 55th International Universities Power Engineering Conference (UPEC), Turin, Italy, 1–4 September 2020; pp. 1–6. [CrossRef]
39. Ratheiser, P.A.; Schichler, U. Qualification of MVAC XLPE cables for DC operation. In Proceedings of the 22nd International Symposium on High Voltage Engineering (ISH 2021), Xi'an, China, 21–26 November 2021; Volume 2021, pp. 179–184. [CrossRef]
40. Buchner, A.; Schichler, U. Review of CIGRE TB 496 regarding Prequalification Test on Extruded MVDC Cables. In Proceedings of the Nordic Insulation Symposium, Trondheim, Norway, 13–15 June 2019. [CrossRef]
41. Beddard, A.; Barnes, M. HVDC cable modelling for VSC-HVDC applications. In Proceedings of the 2014 IEEE PES General Meeting | Conference & Exposition, National Harbor, MD, USA, 27–31 July 2017; pp. 1–5. [CrossRef]
42. NKT. Medium Voltage Cables with XLPE Insulation: Datasheet NA2XSY 12/20. Available online: https://www.nkt.com/products-solutions/medium-voltage/medium-voltage-cables/na2xs2y-12-20-kv (accessed on 12 December 2024).
43. Südkabel GmbH. *Single-Core VPE-Insulated Cables for Medium Voltage Networks*; Südkabel GmbH: Mannheim, Germany, 2021.
44. IEEE. IEEE Task Force on Turbine-Governor Modeling. In *Dynamic Models for Turbine-Governors in Power System Studies*; Technical Report; IEEE: Piscataway, NJ, USA, 2013.

45. *421.1-1986*; IEEE Standard Definitions for Excitation Systems for Synchronous Machines. IEEE: Piscataway, NJ, USA, 1986. [CrossRef]
46. CIM Users Group. Common Information Model for Power System Dynamics—Standard Dynamic Model Reference Document. 2008. Available online: https://www.google.com/url?sa=t&source=web&rct=j&opi=89978449&url=https://cimug.ucaiug.org/Projects/Projects/Dynamics/Standard_Model_TF/Standard%2520Model%2520Reference%2520Manual/CIMdynamics-Model_Reference_28Oct2008.pdf&ved=2ahUKEwjGouLPpruLAxVw2QIHHaM8BQwQFnoECBoQAQ&usg=AOvVaw1LMiCqcjJgz6Cx91nuRI2p (accessed on 12 December 2024).
47. CIGRE WG B4.76. *DC-DC Converters in HVDC Grids and for Connections to HVDC Systems: CIGRE Technical Brochure 827*; Technical Report; CIGRE: Paris, France, 2021.
48. Engel, S.P.; Stieneker, M.; Soltau, N.; Rabiee, S.; Stagge, H.; de Doncker, R.W. Comparison of the Modular Multilevel DC Converter and the Dual-Active Bridge Converter for Power Conversion in HVDC and MVDC Grids. *IEEE Trans. Power Electron.* **2015**, *30*, 124–137. [CrossRef]
49. Soltau, N.; Siddique, H.A.B.; de Doncker, R.W. Comprehensive modeling and control strategies for a three-phase dual-active bridge. In Proceedings of the 2012 International Conference on Renewable Energy Research and Applications (ICRERA), Nagasaki, Japan, 11–14 November 2012; pp. 1–6. [CrossRef]
50. Berger, M.; Kocar, I.; Fortin-Blanchette, H.; Lavertu, C. Hybrid Average Modeling of Three-Phase Dual Active Bridge Converters for Stability Analysis. *IEEE Trans. Power Deliv.* **2018**, *33*, 2020–2029. [CrossRef]
51. Oeding, D.; Oswald, B.R. *Elektrische Kraftwerke und Netze*, 8th ed.; Springer: Berlin/Heidelberg, Germany, 2016.
52. Alvarez, R.; Wahle, M.; Gambach, H.; Dorn, J. Optimum semiconductor voltage level for MMC submodules in HVDC applications. In Proceedings of the 2016 18th European Conference on Power Electronics and Applications (EPE'16 ECCE Europe), Karlsruhe, Germany, 5–9 September 2016; pp. 1–9. [CrossRef]
53. Merlin, M.M.C.; Green, T.C. Cell capacitor sizing in multilevel converters: Cases of the modular multilevel converter and alternate arm converter. *IET Power Electron.* **2015**, *8*, 350–360. [CrossRef]
54. van Hertem, D.; Liang, J.; Gomis-Bellmunt, O. (Eds.) *HVDC Grids: For Offshore and Supergrid Future*; IEEE Press Series on Power Engineering; IEEE Press Wiley and IEEE Xplore: Piscataway, NJ, USA, 2016; Volume 51. [CrossRef]
55. Richter, J.; Resch, S.; Mehlmann, G.; Luther, M. An Enhanced Ideal Transformer Method to Integrate Low-Voltage Power Hardware in Arbitrary Voltage Levels. In Proceedings of the 2023 IEEE Power and Energy Society General Meeting (PESGM), Orlando, FL, USA, 16–20 July 2023; pp. 1–5. [CrossRef]
56. Henninger, S.; Jaeger, J. Advanced classification of converter control concepts for integration in electrical power systems. *Int. J. Electr. Power Energy Syst.* **2020**, *123*, 106210. [CrossRef]
57. Schroeder, M.; Henninger, S.; Jaeger, J.; Ras, A.; Rubenbauer, H.; Leu, H. Integration of batteries into a modular multilevel converter. In Proceedings of the 2013 15th European Conference on Power Electronics and Applications (EPE), Lille, France, 2–6 September 2013; pp. 1–12. [CrossRef]
58. Richter, M.; Mehlmann, G.; Luther, M. Grid Code Compliant Modeling and Control of Modular Multilevel Converters during Unbalanced Faults. In Proceedings of the 2019 54th International Universities Power Engineering Conference (UPEC), Bucharest, Romania, 3–6 September 2019; pp. 1–6. [CrossRef]
59. Sidik, Y.F.; Hu, J.; Joebges, P.; Averous, N.R.; de Doncker, R.W. Control Strategies and Evaluation of Modular Dual-Active Bridge for DC Collector Grid in Offshore Wind Parks. In Proceedings of the 2020 IEEE 9th International Power Electronics and Motion Control Conference (IPEMC2020-ECCE Asia), Nanjing, China, 29 November–2 December 2020; pp. 1522–1529. [CrossRef]
60. NGESO. *Draft Grid Code – Grid Forming Converter Specification 3rd September 2020*; NGESO: London, UK, 2020.
61. North American Electric Reliability Corporation Grid forming technology: Bulk power system reliability considerations. In *White Paper: Grid Forming Controls*; North American Electric Reliability Corporation: Atlanta, GA, USA, 2021.
62. Christensen, P.; Andersen, G.; Seidel, M.; Bolik, S.; Engelken, S.; Knueppel, T.; Krontiris, A.; Wuerflinger, K.; Buelo, T.; Jahn, J. *High Penetration of Power Electronic Interfaced Power Sources and the Potential Contribution of Grid Forming Converters*; Technical Report; ENTSO-E: Brussels, Belgium, 2020.
63. Chen, Y.; Hesse, R.; Turschner, D.; Beck, H.P. Comparison of methods for implementing virtual synchronous machine on inverters. *Renew. Energy Power Qual. J.* **2012**, *10*, 734–739. [CrossRef]
64. Zhong, Q.C.; Weiss, G. Synchronverters: Inverters That Mimic Synchronous Generators. *IEEE Trans. Ind. Electron.* **2011**, *58*, 1259–1267. [CrossRef]
65. Liu, N.; Wang, H.; Sun, L.; Zhou, W.; Song, J.; Zhou, D.; Wang, W.; Chen, Z. Modular Impedance Modeling and Stability Analysis of Hybrid AC/DC Power Systems With Grid-Forming and Grid-Following Converters. *IEEE Access* **2024**, *12*, 4063–4077. [CrossRef]
66. Arévalo-Soler, J.; Nahalparvari, M.; Groß, D.; Prieto-Araujo, E.; Norrga, S.; Gomis-Bellmunt, O. Small-Signal Stability and Hardware Validation of Dual-Port Grid-Forming Interconnecting Power Converters in Hybrid AC/DC Grids. *IEEE J. Emerg. Select. Top. Power Electron.* **2024**. [CrossRef]

67. Bakeer, A.; Chub, A.; Abid, A.; Zaid, S.A.; Alghamdi, T.A.H.; Salama, H.S. Enhancing Grid-Forming Converters Control in Hybrid AC/DC Microgrids Using Bidirectional Virtual Inertia Support. *Processes* **2024**, *12*, 139. [CrossRef]
68. Subotic, I.; Gros, D. Power-Balancing Dual-Port Grid-Forming Power Converter Control for Renewable Integration and Hybrid AC/DC Power Systems. *IEEE Trans. Control Netw. Syst.* **2022**, *9*, 1949–1961. [CrossRef]
69. Mota, D.D.S.; Banda, J.K.; Adeyemo, A.A.; Tedeschi, E. Harmonic-Invariant Scaling Method for Power Electronic Converters in Power Hardware-in-the-Loop Test Beds. *IEEE Open J. Ind. Appl.* **2023**, *4*, 139–148. [CrossRef]
70. Huerta, F.; Gruber, J.K.; Prodanovic, M.; Matatagui, P. Power-hardware-in-the-loop test beds: Evaluation tools for grid integration of distributed energy resources. *IEEE Ind. Appl. Mag.* **2016**, *22*, 18–26. [CrossRef]
71. Li, B.; Xu, Z.; Wang, S.; Han, L.; Xu, D. Interface Algorithm Design for Power Hardware-in-the-loop Emulation of Modular Multilevel Converter Within High-Voltage Direct Current Systems. *IEEE Trans. Ind. Electron.* **2021**, *68*, 12206–12217. [CrossRef]
72. *519^T M-2022*; IEEE Standard for Harmonic Control in Electric Power Systems. (Revision of IEEE Std 519-2014); IEEE: Piscataway, NJ, USA, 2022. [CrossRef]
73. Zhong, Q.C.; Konstantopoulos, G.C. Current-Limiting Droop Control of Grid-Connected Inverters. *IEEE Trans. Ind. Electron.* **2017**, *64*, 5963–5973. [CrossRef]
74. Fan, B.; Liu, T.; Zhao, F.; Wu, H.; Wang, X. A Review of Current-Limiting Control of Grid-Forming Inverters Under Symmetrical Disturbances. *IEEE Open J. Power Electron.* **2022**, *3*, 955–969. [CrossRef]
75. Taul, M.G.; Wang, X.; Davari, P.; Blaabjerg, F. Current Limiting Control With Enhanced Dynamics of Grid-Forming Converters During Fault Conditions. *IEEE J. Emerg. Sel. Top. Power Electron.* **2020**, *8*, 1062–1073. [CrossRef]
76. Qoria, T.; Gruson, F.; Colas, F.; Kestelyn, X.; Guillaud, X. Current limiting algorithms and transient stability analysis of grid-forming VSCs. *Electr. Power Syst. Res.* **2020**, *189*, 106726. [CrossRef]
77. Kamalhosseini, S.; Burlakin, I.; Kuri, A.; Mehlmann, G.; Luther, M. Grid-Forming Capability of Power Plant Control: Optimization Through Battery Energy Storage Integration. In Proceedings of the 23rd Wind & Solar Integration Workshop, Helsinki, Finland, 8–11 October 2024.